Analytica Chimica Acta 835 (2014) 1–18

Contents lists available at ScienceDirect

Analytica Chimica Acta

journal homepage: www.elsevier.com/locate/aca

Review

Bioimaging mass spectrometry of trace elements – recent advance and applications of LA-ICP-MS: A review

J.Sabine Becker [a,*], Andreas Matusch [b], Bei Wu [a]

[a] Central Institute for Engineering, Electronics and Analytics (ZEA-3), Forschungszentrum Jülich, Jülich D-52425, Germany
[b] Institute for Neuroscience and Medicine (INM-2), Forschungszentrum Jülich, Jülich D-52425, Germany

HIGHLIGHTS

- Bioimaging LA-ICP-MS is established for trace metals within biomedical specimens.
- Trace metal imaging allows to study brain function and neurodegenerative diseases.
- Laser microdissection ICP-MS was applied to mouse brain hippocampus and wheat root.

GRAPHICAL ABSTRACT

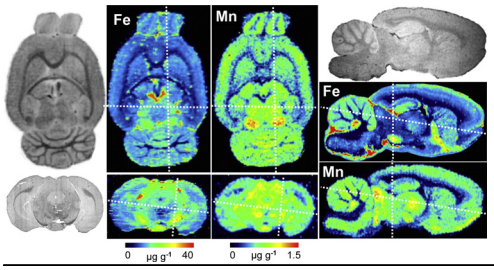

ARTICLE INFO

Article history:
Received 10 June 2013
Received in revised form 18 April 2014
Accepted 19 April 2014
Available online 26 April 2014

In memoriam of Hans-Joachim Dietze (10.11.1935–27.02.2014)

Keywords:
Elemental bio-imaging
Laser ablation inductively coupled plasma mass spectrometry
LA-ICP-MS
Trace metal imaging

ABSTRACT

Bioimaging using laser ablation inductively coupled plasma mass spectrometry (LA-ICP-MS) offers the capability to quantify trace elements and isotopes within tissue sections with a spatial resolution ranging about 10–100 μm. Distribution analysis adds to clarifying basic questions of biomedical research and enables bioaccumulation and bioavailability studies for ecological and toxicological risk assessment in humans, animals and plants. Major application fields of mass spectrometry imaging (MSI) and metallomics have been in brain and cancer research, animal model validation, drug development and plant science. Here we give an overview of latest achievements in methods and applications. Recent improvements in ablation systems, operation and cell design enabled progressively better spatial resolutions down to 1 μm. Meanwhile, a body of research has accumulated covering basic principles of the element architecture in animals and plants that could consistently be reproduced by several laboratories such as the distribution of Fe, Cu, Zn in rodent brain. Several studies investigated the distribution and delivery of metallo-drugs in animals. Hyper-accumulating plants and pollution indicator organisms have been the key topics in environmental science. Increasingly, larger series of samples are analyzed, may it be in the frame of comparisons between intervention and control groups, of time kinetics or of three-dimensional atlas approaches.

Contents

1. Introduction . . . 2
   1.1. Motivation for element imaging in biological tissues – example brain . . . 3
   1.2. Position of MSI by LA-ICP-MS amongst other methods . . . 3
   1.3. Principle of MSI by LA-ICP-MS . . . 3
2. Advance in methodology of LA-ICP-MS tissue imaging . . . 6
   2.1. Sample preparation . . . 6

* Corresponding author. Tel.: +49 2461 612698; fax: +49 2461 612560.
E-mail addresses: s.becker@fz-juelich.de (J.S. Becker), a.matusch@fz-juelich.de (A. Matusch), b.wu@fz-juelich.de (B. Wu).

http://dx.doi.org/10.1016/j.aca.2014.04.048
0003-2670/

2.1.1. Native tissue . . . 6
2.1.2. Limited usefulness of fixed tissue . . . 6
2.2. Calibration . . . 7
2.2.1. External standards . . . 7
2.2.2. Internal standards . . . 7
2.3. Operation and ablation modes . . . 9
2.3.1. Ablation modes . . . 9
2.3.2. Minimization/resolution of polyatomic isobaric interferences . . . 10
2.4. Data treatment . . . 10
2.5. Improvement of spatial resolution . . . 10
2.5.1. Commercial ablation systems . . . 10
2.5.2. LMD-LA-ICP-MS . . . 11
2.5.3. Other approaches for improving spatial resolution . . . 11
3. Applications of LA-ICP-MS bio-imaging – 10 years of work . . . 11
3.1. Element-architecture in healthy organisms . . . 11
3.1.1. Animal tissue . . . 11
3.1.2. Human biopsy/autopsy tissue . . . 12
3.1.3. Plants . . . 12
3.1.4. Non-vertebrates . . . 12
3.2. Tissue at pathological conditions . . . 12
3.2.1. Biopsy/autopsy specimens . . . 12
3.2.2. Experimentally induced disease . . . 12
3.3. Organisms after exposition to metal/hetero-element compounds at lifetime . . . 12
3.3.1. Hyper- and hypo-accumulating plants . . . 12
3.3.2. Development of drugs, therapeutic nanoparticles, contrast agents and their delivery . . . 13
3.3.3. Stable isotope tracer studies . . . 13
3.3.4. Other . . . 13
3.4. Ex vivo binding/staining including immunhistochemistry . . . 13
3.4.1. Immunhistochemistry/histological stains . . . 13
3.4.2. Ex vivo binding studies of element species of interest . . . 14
3.5. Various cases . . . 14
3.5.1. Teeth . . . 14
3.5.2. Leaves, co-planar . . . 14
3.5.3. Root blots of plants during growth . . . 14
3.6. Larger numbers of serial samples/group comparisons and kinetics . . . 14
3.7. Atlas approaches/3D reconstruction of serial sections . . . 15
3.7.1. Atlas of formalin fixed mouse brain . . . 15
3.7.2. Wheat grain germ atlas . . . 15
4. Conclusions . . . 15
Acknowledgements . . . 15
References . . . 15

Dr. J. Sabine Becker is the head of the BrainMet (Bioimaging of Metals in Brain and Metallomics) at Research Centre Juelich, Germany. She has more than 35 years of extensive experience in all fields of mass spectrometry and pioneered imaging LA-ICP-MS for micro- and nanolocal analysis for biological specimens combined to metallomics. Dr. Becker is the author of the comprehensive handbook: Inorganic Mass Spectrometry: Principles and Applications, Wiley, 2007, of 355 scientific publications, 24 patents and is IUPAC Fellow and member of several Editorial/Advisory Boards of the *International Journal of Mass Spectrometry*, *Journal of Analytical Atomic Spectrometry*, *Talanta*, *Metallomics* and others.

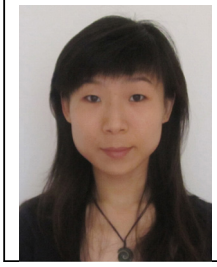

Bei Wu received her PhD in Environmental Engineering at Zhejiang University, China, in 2009. After working as an Alexander von Humboldt postdoctoral fellow, she was a scientific coworker at the BrainMet laboratory at Forschungszentrum Jülich (FZJ), Germany, working on the development of LA-ICP-MS imaging of metals/metalloids with high spatial resolution down to the low- and sub-μm range. Her forthcoming research activities will investigate elemental cycling in soil system using advanced mass spectrometric techniques in the Institute of Bio- and Geosciences, FZJ.

Dr Andreas Matusch studied medicine and physics at the universities of Marburg, Munich, Poitiers and Paris-VI. He received his MD in medicine in 2000 followed by clinical education in Neurology in Paris. Since 2003 he has worked at Forschungszentrum Jülich in the field of molecular neuroimaging using mass spectrometric and radiotracer techniques at the translational junction of medicine, analytical and nuclear chemistry. He contributed analytical questions and samples of clinical relevance, implemented experience from medical tissue and data processing and assured data analysis bridging from precise morphology to function.

1. Introduction

Interest in studying elemental – especially trace metal – distributions in biological tissues is progressively growing. A good ten years ago Kindness et al. published the inaugural study introducing laser ablation inductively coupled plasma mass spectrometry imaging (MSI by LA-ICP-MS) for this purpose [1]. Since then this technique has been set up in a good twenty laboratories worldwide. Meanwhile about 88 studies (Table 1) were published that investigated native biological structures by imaging LA-ICP-MS, of these 56 in 2011 and thereafter. Therefore, while emphasizing aspects emerging from very recent studies and oriented on application the exclusive subject of this review is bio-imaging by LA-ICP-MS. General principles are introduced only briefly (Figs. 1 and 2). Earlier work has been reviewed elsewhere [2–4]. Initially and still mostly LA-ICP-MS has been applied for surface analysis of solid matter in material science and its branches in engineering, geology, archeology, analysis of fossils etc., In the biosciences there is a body of excellent work applying single shot [5] or line scan [6] LA-ICP-MS as well as imaging of electrophoresis gels or blots [7]. Here exclusively imaging of intact tissue is regarded. While other reviews compared different element imaging techniques [3,4] or different mass spectrometry imaging techniques for a dedicated field of biological application, here only MSI by LA-ICP-MS is considered. Examples chosen for illustration were in part new figures derived from published studies (Figs. 3 and 4) to another part so far unpublished work (Figs. S1–S5).

1.1. Motivation for element imaging in biological tissues – example brain

Metals such as Cu, Zn, Fe, Na, Ca, K, Mn, Mg and others are required for cell development and survival. Co, Mn, Cu, Fe, Zn are necessary as cofactors for enzymes of basal cell metabolism such as the respiratory chain and for oxygen transport [8]. Localization and binding of metals are paramount for proper function as e.g., free Fe^{2+} or Cu^{+} catalyze the formation of hydroxyl radicals from H_2O_2 via the fenton reaction [9]. The aforementioned features apply in general and are especially critical for brain function as the brain is the organ with the highest energy demand and the lowest compensatory reserve towards damage. Metals obviously have a certain tropism to the brain. Nutritional and genetically-induced deficiencies of essential metals are known to comprise neuro-psychiatric symptoms (such as developmental delay and seizures in Menkes Cu deficiency disease or irritability and pica in sideropenia). The stabilization of abnormal proteins or the generation of metal-containing deposits as pathological feature of Alzheimer's or Parkinson's disease has been closely linked to a metal dys-balance in the brain [9,10]. As the brain is highly morphologically organized into fine branched and layered structures showing highly differentiated functions and highly differentiated metal distributions the brain has been a highyielding object for the application of spatially resolved chemical analytical techniques.

The neurotoxicity of heavy metals such as Pb, Cd or Hg, as well as excessive Mn, Cu or Zn known since a long time, could progressively be braked down to specific interaction with molecular targets in the recent years [11,12]. For instance, Pb^{2+} blocked L-type Ca^{2+} channels at $K_i = 30$ nM and blocked synaptotagmin, a protein which mediates the Ca^{2+} induced exocytosis of neurotransmitter vesicles, at $EC_{50} = 8$ nM [11]. Cd^{2+} blocked the tetrodotoxin insensitive Na^{+} channel at $K_i = 200$ nM [11] and iNOS at $IC_{50} = 220$ nM [11]. Hg^{2+} blocked the kainate receptor (a Na^{+}/K^{+} channel) at $IC_{50} = 70$ nM [13]. Cu^{2+} physiologically blocks $GABA_A$ receptors at $IC_{50} = 35$ nM [14] and Zn^{2+} the NR2A subunit of NMDA receptors at $IC_{50} = 15$ nM [11]. All these pathological and toxicological processes are again highly locally differentiated. Localization of physiological or toxic metal enrichments may guide identification of relevant molecular inter-actors via correlation with gene expression maps and via targeted sampling of material for biochemical studies.

When it comes to plant science, the principle of Justus von Liebig, that the trace nutrient of lowest availability is growth limiting is common knowledge. In population health nutrient deficiencies are cured by introduction of better crop varieties. Decontamination of soils by hyperaccumulator plants is a recent issue. Here again localization of elements to e.g., the xylem transporting water and micronutrients upward or to the phloem transporting sugars downward or to other differentiated layers and structures is paramount for understanding the function.

1.2. Position of MSI by LA-ICP-MS amongst other methods

Before the emergence and alternatively to MSI by LA-ICP-MS other sensitive microanalytical element imaging techniques with high lateral resolution have been available such as X-ray spectroscopic techniques [15] and secondary ion mass spectrometry (SIMS) [16]. Of these LA-ICP-MS offers the lowest limits of detection at the $\mu g\,g^{-1}$ range and below [3,17]. LA-ICP-MS is comparatively matrix insensitive, offers wide multiplex capabilities and a particular wide concentration dynamical range. In typical bio-imaging experiments on 30 μm tissue sections the highest isotope concentration observed was 10,000 $\mu g\,g^{-1}$ ^{39}K and the lowest limit of detection 0.0005 $\mu g\,g^{-1}$ of ^{208}Pb when using 50 μm laser spotsize and a quadrupole instrument.

With respect to conventional biological tissue sections of typically 5–30 μm, SIMS provides excellent spatial resolution, down to 50 nm but no valid element quantification as its penetration depth is only some 0.2–10 nm (1 μm can be reached in depth profiling experiments), because the sample thickness is highly inconstant and because of considerable matrix effects. The strength of SIMS are rather semi-quantitative localization studiesand isotope ratio imaging in very small objects down to subcellular level in thin sections of about 300 nm as prepared forelectron microscopy (such as cross sections through plant sprouts).

X-ray fluorescence (XRF) requires mounting of tissue sections onto plastic foil supports. Spectral interferences together with the low energy resolution of the most widely used energy dispersive X-ray detectors (EDX), background from scatter and abundant matrix elements limit sensitivity and quantification. The energy range provided by a given set-up and the Be-window of most detectors further limit the set of analytes accessible. When an X-ray tube is the excitation beam source also scattered bremsstrahlung and characteristic lines of the anode material add to the background. In some comparative studies identical samples were imaged by LA-ICP-MS vs. synchrotron-μXRF [18], vs. benchtop-XRF [19], vs. SIMS [20] and vs. proton induced X-ray emission (PIXE) [21].

1.3. Principle of MSI by LA-ICP-MS

In LA-ICP-MS a commercial laser ablation system is coupled to a sensitive ICP-MS. An analytical workflow of MSI by LA-ICP-MS is exemplified in Fig. 1. The focused laser beam from the laser ablation system is used to scan the tissue sections. The ablated material is then transported with the carrier gas – Ar or mixtures of Ar and He – in the ICP source of the ICP-MS where it is then ionized. The ions within a mass range of interest are separated by their mass-to-charge ratio and detected by the detection system of the mass spectrometer.

Ion intensities of each analyte are recorded against time along the course of laser scanning. These raw data of an LA-ICP-MS imaging experiment are then reconstructed to images, eventually calibrated, visualized and can be subdued to further image treatment algorithms.

Table 1
Overview of the work applying LA-ICP-MSI to biological tissues.

Sample	1)	*n*	2)	Elements recorded (LOD, $\mu g\,g^{-1}$)	Pixel dimensions*	Year	Ref.
P.A. Doble, D.J. Haare et al., Sydney, Australia				New wave UP213 (25 cm × 25 cm cell), Agilent 7500cx (Q)**			
6-OHDA mouse brain section	n	3 + 1	q	C, P, Mn, Fe, Cu, Zn	$8 \times 12\,\mu m^2$	2009	[38]
Biopsy specimens of lymph nodes with metastatic melanoma	f	1 + 1	n	C, P, S, Fe, Cu, Zn	$32 \times 40\,\mu m^2$	2009	[78]
Biopsy specimens of knee cartilage	n	1	n	(H_2 reaction) C, Mg, P, Ca, Zn, Sr	$32 \times 29\,\mu m^2$	2009	[91]
Biopsy specimens of nuclear workers	f	4	q	Th, U, Pu	$9 \times 30\,\mu m^2$	2010	[105]
6-OHDA mouse brain series of 12 sections ("3D")	n	1	q	C, P, Mn. Fe, Cu, Zn	$60 \times 100\,\mu m^2$	2010	[23]
Human teeth	n	3	n	C, P, Ca, Mn, Zn, Sr, Cd, Pb	$16 \times 20\,\mu m^2$	2011	[114]
Human teeth	n	3	n	P, Ca, Zn, Sr, Cd, Pb	$18 \times 30\,\mu m^2$	2011	[110]
4/5 Mouse brain atlas 44 coronal 30 μm sections (of ca. 300)	f	1		C, Fe, Cu, Zn, I	$78 \times 80\,\mu m^2$ (×150 μm)	2012	[37]
Mouse brain, optimization of collision cell conditions	f	1	q	H_2C, Mn, Fe, Co, Cu, Zn	$30 \times 30\,\mu m^2$	2012	[52]
Preparation of sheep brain homogenate standards coronal mouse brain section (n),	n	1	q	C, Mg (25), Mn (0.9), Fe (13), Co (0.5), Cu (2.2), Zn (3.1), Se (5.2), Sr (1.2)	$40 \times 100\,\mu m^2$	2013	[31]
Children, monkey and neanderthal teeth	n	25 + 5	n	Ba, Ca, Sr, Y, La, Ce, Nd, Sm, Eu, Yb, Th, U	$30 \times 30\,\mu m^2$	2013	[40]
Mouse exposed to intermittent hypoxia vs. control	f	5 + 6	q	C, P, Mn, Fe, Co, Cu, Zn	$30 \times 30\,\mu m^2$	2013	[115]
J. Feldmann et al., Aberdeen, UK				Cetac LSX-200, LECO-Renaissance (ToF), cooled ablation cell			
Sheep liver	n	2	n	C, Cu, Zn	$100 \times 300\,\mu m^2$ (raster)	2003	[1]
				UP-213/NWR 213 or Cetac LSX-200, Agilent 7500c (Q)			
Liver abscesses in mice deficient for endogeneous Zn/Mn chelator	n	3 + 3	n	C, Mg, P, S, Ca, Mn, Fe, Cu, Zn	$25 \times 100\,\mu m^2$	2008	[93]
Shotgun projectiles in rat hind limbs	n	1	n	C, P. S, Cu, Zn, Sn, Pb, Bi	$23 \times 150\,\mu m^2$	2012	[104]
wounded spruce bark	f	3 + 3	n	C, Mg, Al, P, S, K, Ca, Mn, Fe, Cu, Zn	$7 \times 250\,\mu m^2$	2012	[92]
^{67}Zn and ^{70}Zn double tracer study in rats	n	10	n	C, SI, P, S, Mn, Zn, Ge	$58 \times 160\,\mu m^2$	2012	[24]
C. McLeod, J. Bunch, Hutchinson R.W. et al., Sheffield, UK				UP-266, Cetac LSX-200, Agilent 4500 (Q)			
Eu tagged AB and Ni enhanced DAB in Alzheimer mouse brain	f	2	n	Mg, Al, Ca, Fe, Ni, Cu, Zn, Eu	$36 \times 100\,\mu m^2$	2005	[46]
Au/Ag AB in human gut and breast cancer and tissue microarrays	f	3	n	Ag, Au	$1 \times 10\,\mu m^2$	2008	[77]
Gd nanoparticles in mouse tumor and kidney	n	1	n	Zn, Gd	$25 \times 50\,\mu m^2$	2010	[25]
Gd in tumor and brain, standard development	f	2 + 1	q	C, Fe, Zn, Sr (0.24), Gd (0.003), Pt (0.005)	$28 \times 300\,\mu m^2$	2011	[34]
local infusion of Gd and Pt into mouse and pig brain	f	6 + 1	n	C, Fe, Zn, Gd, Pt	$30 \times 310\,\mu m^2$	2012	[22]
Gd and Pt local infusion into mouse and pig brain	f	22 + 1	q	C, Fe, Zn, Gd, Pt	$23 \times 720\,\mu m^2$	2012	[23]
Receptor targeted DNA delivery nanoparticles in rat brain	n	32	n	Fe, Gd	$\approx 30 \times 310\,\mu m^2$	2013	[66]
T. Prohaska et al., Vienna, Austria				UP-193, ELAN 6100 DRCe (Q)/Nu Plasma HR (sf)**			
Root cross sections of Ni hyper-accumulator plants	n	2	q	Mg, Ni, Fe	$10 \times 75\,\mu m^2$	2010	[94]
Metabolic monitoring of plant roots, blots of flat chamber	n	2	q	N, P (0.003), Fe	$50 \times 333\,\mu m^2$	2012	[112]
C. F. Wang et al. , Taiwan				UP-213, Agilent 7500a (Q)			
Locally injected Iron oxide/Gd nanopartcle mouse prostate cancer	n	1	n	C, P, S, Fe, Ni, Cu, Zn, Gd	$72 \times 100\,\mu m^2$	2011	[100]
CdSe quantum dots in mouse spleen and liver	n	4	n	P, Fe, Cu, Zn, Se, Cd	$90 \times 110\,\mu m^2$ (sz)	2012	[101]
Element imaging in honeybees and larvae	n	3	q	Mg, P, S, Ca, Mn, Fe, Cu, Zn, Pb	$100 \times 110\,\mu m^2$	2013	[56]
D. Günther et al., Zürich, Switzerland				193 nm ArF eximer laser (Lambda-Physik), tube cell, He, ThermoElement 2 (sf)			
Ho-tagged HER2-antibodies on breast cancer	f	1	n	Ho (0.01)	$1 \times 1\,\mu m^2$ (1 sz)	2013	[49]
				ArF excimer, Geo Las C, CyTOF ICP-ToF			
Lanthanide tagged antibodies on breast cancer		21	n	32 different Lanthanide isotopes (0.01)	$1 \times 1\,\mu m^2$ (1 sz)	2014	[54]
B. Jackson et al., Dartmouth College, Hanover, NH, USA				UP-213, Elan 6100 DRC+			
Coronal rat brain sections	n + f	2	q	C, P, S, Fe (3.6), Cu (0.12), Zn (0.66)	$61 \times 100\,\mu m^2$	2006	[26]
				UP213, Agilent 7500cx			
CdSe/ZnS Quantum dots in amphipoda	f	>4	n	(H_2 reaction) Ca, Zn, Se, Cd	$40 \times 40\,\mu m^2$	2012	[48]
U. Karst et al., Münster, Germany				Cetac-LSX213, Thermo iCAP Qc, He			
Combined LA-ICP-MS and APCI-MS imaging, Pt, Br, in kidney	f	1	n	Al, Sc, Br, Pt, Tl	$13 \times 25\,\mu m^2$	2013	[99]
Mouse cochlea, kidney, testis after chronic Pt and washout	f	1	q	Ir, Pt, Bi	$20 \times 10\,\mu m^2$	2013	[98]
Human resected visceral specimens, HE stained	f	4	n	C, Al, Br, Pt	$31 \times 10\,\mu m^2$	2013	[76]
Mn uptake into caenorhabdidis elegans DJ1 knock out mutant	n	4	n	Mn, 10 ppt Rh nebulization, He collision	$4 \times 4\,\mu m^2$	2014	[116]
Metal release in tissue by an Ag coated TiV alloy implant, μXRF	f	1	n	Al, Ti, V, Zr, Ag	$25 \times 25\,\mu m^2$ (sz 25)	2014	[19]
J. T. Van Elteren, Ljubljana, Slowenia				UP-213, Agilent 7500ce, He			
Hg in maize root cross sections	n	1	q	Hg	$20 \times 20\,\mu m^2$ (raster)	2014	[35]
Flowers, pollen and seeds of a halophyte plant, Zn or NaCl feed	n	3	n	Na, K, Ca, Zn	$60 \times 55\,\mu m^2$	2013	[96]
Leaves of Zygophyllum grown with Cd, Zn, Ctrl., PIXE, EXAFS	n	1	n	Mg, P, S, K, Ca, N, Fe, Zn, Cd	$8 \times 8\,\mu m^2$	2014	[21]
F. Vanhaecke, A. Izmer, Ghent, Belgium				UP-213, Agilent 7500cs, He			
Water flea (daphnia) LA-ICP-MS vs. μXRF	f	1	n	C, P, S, Cl, K, Ca(110), Cu (9), Zn (11)	$15 \times 15\,\mu m^2$	2010	[18]
				UP-193HE, Thermo Element XR			
Br-drug TMC207 after 1, 4, 8 h in rat entire body sections	f	1	q	Br	$200 \times 200\,\mu m^2$	2012	[103]
Water flea (daphnia) exposed to enriched ^{64}Zn tracer	f	1	n	Cu, Zn	$30 \times 30\,\mu m^2$	2013	[89]

Table1 (*Continued*)

Sample	1)	*n*	2)	Elements recorded (LOD, $\mu g\,g^{-1}$)	Pixel dimensions*	Year	Ref.
A. Sanz-Medel, Oviedo, Spain				LSX-213, Thermo Element 2 (sf), He			
Human eye's anterior chamber angle, sputtered Au int, standard	f	10	n	C, Mg, Fe, Cu, Au	$42 \times 10\,\mu m^2$	2013	[45]
Cryogenic cell, plant leave, eye section	n	2	n	Fe, Cu, Zn, I	$8 \times 20\,\mu m^2$ (sz 10)	2014	[61]
Depth profiling in frozen hydrated human eye lens, cryogenic-cell	n	1	q	Fe, Cu, Zn, Au	$23 \times 70\,\mu m^2$ (sz 50)	2014	[62]
M.A.Z. Arruda et al., Campinas, Brazil				UP-213, Elan DRC-e			
Leaves of selenit feed sunflowers	n	3	q	(O_2 reaction) C, SO^+, SeO^+	$22 \times 300\,\mu m^2$	2013	[53]
Y. Zhu et al., Ibaraki, Japan				UP-213, Agilent 7700x			
Peanut seads	n	3	n	C, Mg, P, K, Mn, Fe, Cu, Zn, Rb, Sr, Mo, Ba	$18 \times 100\,\mu m^2$	2012	[84]
N. Jakubowski et al., BAM, Berlin, Germany				NWR213, Thermo Element XR, He			
Rat kidney after single dose Pt treatment and 5 days whashout	f	4	n	Cu, Zn, Pt (50 fg)	$5 \times 8\,\mu m^2$ (sz)	2011	[58]
Iodine stain of culture cells and liver, Ho-Her2 AB on breast cancer	f	3	n	I, Eu, Ho, Tm	$5\,\mu m\,s^{-1} \times 4\,\mu m$ (sz)	2011	[108]
Multiplex Ho, Tm, Tb-tagged antibodies on breast cancer	f	3	n	Eu, Tb, Ho, Tm	$25 \times 25\,\mu m^2$	2011	[107]
Au and Ag nanoparticles in adherent single cells	f	4	n	Au, Ag	$5 \times 6\,\mu m^2$	2012	[102]
D. Amarasiriwardena et al., Amherst, MA, USA				NWR-213, Elan 6000a, He			
Roots of fern grown on contaminated soil	n	5	n	C, Cu, Zn, Sb, Pb	$32 \times 40\,\mu m^2$	2012	[95]
Au-nanoparticles in roots of rice	n	4	q	C, Au	$2 \times 25\,\mu m^2$	2013	[39]
G. Verbeck et al., Denton, TX, USA				NWR-213, Varian 820 (Q)			
Localization of Hg to macrophage aggregates in fish (gar) liver	f	7	n	Se, Hg	$100 \times 100\,\mu m^2$	2011	[113]
P. Babula et al., Brno, Czech R.				UP-213, Agilent 7500 CE, He			
Pepper leaves, control and 7d-Pb feed, LIBS vs. LA-ICP-MS	n	3	n	K, Pb	$200 \times 200\,\mu m^2$	2011	[117]
B. Li et al., Beijing, China				UP213, Thermo Element 2			
Cross section through the stem of Indian mustard	n	1	n	P, S, K, Ca, Cu, Zn, Cd	$20 \times 30\,\mu m^2$ (sz 20)	2014	[97]
J.S. Becker et al., FZ-Jülich, Germany				Ablascop (Bioptic), Element 1			
Native human brain, Hippocampus	n	2	q	P, S, Cu, Zn, Th, U	$37 \times 140\,\mu m^2$ (sz 50)	2005	[80]
Rat brain tumor	n	1	q	P, S, Cu, Zn	$20 \times 375\,\mu m^2$ (sz 50)	2005	[118]
				Cetac LSX 200			
Human brain tumor (glioblastoma) biopsy	n	1	q	Cu, Zn, Pb, U	$50 \times 100\,\mu m^2$ (sz 50)	2006	[119]
Human control brain, reproducibility, variation of spot size	n	1	q	C, Cu, Zn	$40 \times 135\,\mu m^2$ (sz 50)	2007	[120]
Pt in rat kidney after acute cisplatin single dose	n	2	q	Cu, Zn, Pt	$50 \times 100\,\mu m^2$ (sz 50)	2007	[55]
Whole body sections of slugs	n	3	q	C, Cu, Zn, Se	$40 \times 100\,\mu m^2$ (sz 50)	2007	[88]
Rat brain tumor, serial sections, ^{13}C and water content	n + f	5	q	C, P, S, Cu, Zn	$40 \times 167\,\mu m^2$ (sz 50)	2008	[73]
Cortical layering pattern across different regions of human brain	n	1	q	Cu, Zn, Pb	$72 \times 300\,\mu m^2$	2008	[81]
Binding of $(UO_2)^{2+}$ and Nd^{3+} to rat brain sections	n	2	q	Nd, U	$40 \times 100\,\mu m^2$ (sz 100)	2008	[67]
				Cetac LSX 200, large ablation chamber			
Large area $11 \times 6.5\,cm^2$ of human brain hemisphere	n	1	q	Cu, Zn	$300 \times 300\,\mu m^2$	2007	[121]
				Elan 6100, Cetac LSX 200			
Leafs, shoots and roots of tobacco	n	1	q	Mg, Mn, Fe, Cu, Zn, Cd, Rh, Pt, Pb	$300 \times 300\,\mu m^2$	2008	[82]
				Agilent 7500e, New wave UP 266			
Sea snails for environmental monitoring of Cd, Hg, Pb	n	2	q	C, S, Cu, Zn, Cd, Hg, Pb	$60 \times 160\,\mu m^2$ (sz 160)	2009	[106]
Leafs of Cu accumulator plant Elsholtzia, Cu exposition	n	9	q	B, Mg, P, S, K, Mn	$80 \times 460\,\mu m^2$ (sz 160)	2009	[122]
Multielement imaging in rat brain sections, aging	n	2	q	C, Mg, P, S, K, Mn, Fe, Cu, Zn	$55 \times 120\,\mu m^2$ (sz 120)	2010	[42]
MTPT mouse model of Parkinson, at 2 h, 7 days and 28 days	n	18	q	C, P, Mn, Fe, Cu, Zn	$20 \times 120\,\mu m^2$ (sz 120)	2010	[22]
Rat brain photothrombosis (model for stroke)	n	1	q	C, Na, Mg, P, S, Cl, Fe, Cu, Zn	$80 \times 190\,\mu m^2$ (sz 160)	2010	[123]
Hematoma model in rat brain, rat brain tumor	n	2	q	C, Na, Fe, Ni, Cu, Zn	$130 \times 170\,\mu m^2$ (sz 160)	2010	[124]
				Thermo X Series2, New Wave UP266			
Solution based calibration, wet vs. dry plasma, mouse brain	n	1	q	Li, Mn, Fe, Cu, Zn, Rb	$108 \times 330\,\mu m^2$	2010	[43]
Mouse heart, LA-ICP-MS vs. ToF-SIMS	n	2	q	C, Na, Mg, P, S, K, Ti, Mn, Fe, Cu, Zn	$50 \times 160\,\mu m^2$ (sz 160)	2010	[20]
Human mesencephalon	f	2	q	C, P, Ca, Mn, Fe, Ni, Cu, Zn, Cd, Pb	$159 \times 170\,\mu m^2$ (sz 120)	2011	[79]
				Thermo X Series2, New Wave NWR213			
Human brain biopsy material, hippocampus	n	1	q	C, Fe, Cu, Zn	$39 \times 140\,\mu m^2$ (sz 90)	2011	[68]
Rat brain horizontal, segmentation, cluster analysis	n	1	q	C, Na, Mg, P, S, K, Mn, Fe, Cu, Zn, Pb, U	$90 \times 130\,\mu m^2$ (sz 80)	2011	[125]
Unilateral 6-OHDA mouse, combined with lipid MALDI-IM-ToF-MS	n	2/12	q	C, Mn, Fe, Cu, Zn	$83 \times 160\,\mu m^2$ (sz 110)	2012	[32]
Unilateral 6-OHDA mouse model of Parkinson, L-DOPA vs. Ctrl.	n	18	q	C, Mn, Fe, Cu, Zn	$108 \times 110\,\mu m^2$ (sz 80)	2012	[71]
APP single mutant model of Alzheimer, mouse brain	n	4/6	q	C, Mn, Fe, Cu, Zn	$120 \times 160\,\mu m^2$ (sz 120)	2012	[70]
Mouse spinal cord	n	3	q	C, Na, Mg, P, S, Cl, K, Mn, Fe Cu, Zn	$65 \times 65\,\mu m^2$ (sz 60)	2012	[75]
Wheat germ embryo	n	1/34	q	B, C, Na, Mg, P, S, K, Ca, Cl, Mn, Fe, Cu, Zn, Mo	$26 \times 40\,\mu m^2$	2013	[85]
Bovine patella cartilage exposed to Gd-DTPA	n	1	q	C, Na, Mg, P, S, Cl, K, Ca, Ti, Cu, Zn, Gd	$77 \times 90\,\mu m^2$	2013	[109]
Human liver, control cirrhosis	n	10	q	C, Mn, Fe, Cu, Zn, Cd	$70 \times 80\,\mu m^2$ (sz 60)	2013	[90]
Liver of Cu efflux ATPase7B mutant mice	n	5 + 5	q	C, Na, P, S, Cl, Mn, Fe, Cu, Zn, Rb, Mo, Sn, Hg	$70 \times 70\,\mu m^2$ (sz 60)	2013	[126]
				Thermo X Series 2, LMD MMI smart cut plus			
LMD-ICP-MS, variation of spot size, LODs on standards	n + f	2	q	C, Na, Mg, P, K, Fe, Cu, Zn	$4 \times 6\,\mu m^2$ (sz 4)	2011	[127]
LMD-ICP-MS in rat brain hippocampus, ablation chambers	n	2	q	C, Na, Mg, P, K, Fe, Zn	$18 \times 16\,\mu m^2$ (sz 6)	2012	[63]

1) n, native; f, fixed tissue; *n*, number of individuals/animals of which at least an image of one section was available; 2) n, not quantitative, count rates or ratios of count rates determined; q, quantitative, determination of absolute $\mu g\,g^{-1}$ concentrations; *If several scan speeds, integration times and line distances were used for several samples the smallest (best) dimensions are given; **type of mass analyzer: Q, quadrupole; sf, sector field; AB, antibody; He, Helium as initial carrier, addition of Ar downstream; sz, spot size, distance between lines not given.

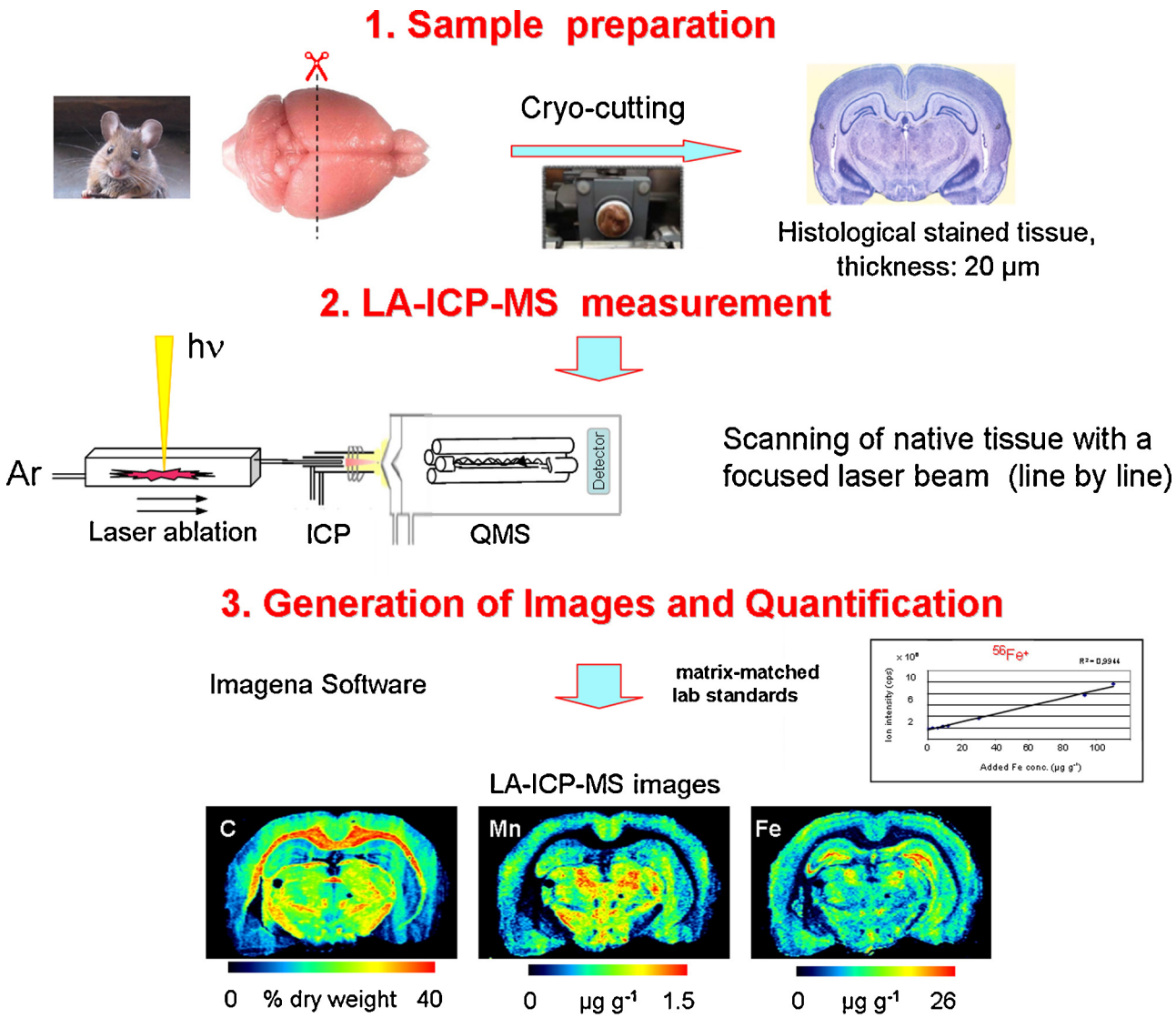

Fig. 1. Analytical workflow of LA-ICP-MS imaging from sample preparation, cryo-cutting of tissue sections, via the mass spectrometric measurements by LA-ICP-MS, to the evaluation of raw data and quantification of analytical results.

2. Advance in methodology of LA-ICP-MS tissue imaging

2.1. Sample preparation

2.1.1. Native tissue

In biology, the element distribution as close as possible to physiological conditions is of key interest. Therefore, native cryo-sections seem the ideal sample material [22–25]. Some adhesion of the section to the glass slide is desired, in order to avoid splintering during ablation. Here Starfrost™ adhesive slides proved optimal while Marienfeld™, gelatin or chrom-alaune coating produced inacceptable background signal and the adhesive capacities of Superfrost™ were suboptimal. Optimally samples are mounted by electrostatic adhesion or short gentle pressure onto pre-cooled slides and progressively thawed from one end to the other by gliding the backside over a finger or the edge of a 37 °C warming plate. Any air bubbles thus are pro-pulsed by the linear or convex thawing front. Samples should be dried at least for 1 h at 37 °C and stored at −80 °C if preservation of proteins is desired, otherwise for element analysis and conventional histological stains dry storage at room temperature is sufficient. As also known from thin layer chromatography, during drying mobile elements are transported to the surface of the section thickness and occasionally also lateral transport leads to drying artifacts (observed for Na, K, Cl). If mobile species are of interest, freeze drying or ablation of the frozen hydrated sample in a cryogenic cell can be the ultimate method. In our own studies exemplified here the tissue was immediately removed, snap frozen in −50 °C isopentane, wrapped after evaporation of isopentane, stored at −80 °C and cryo-cut into 10 μm and 30 μm sections.

2.1.2. Limited usefulness of fixed tissue

A differential washout of analyte species from anatomical structures in aqueous milieu such as in 4% formalin solution is well known and was already documented (but not discussed) in the 2005 paper by Jackson et al. [26] for Fe, Cu and especially for Zn. Recently, a systematic kinetic of element leaching from rat heart throughout 2 h, 1, 2, 4 and 6 days of formaline fixation was published [27]. The formation of formic acid even facilitates the washout of di- or higher valent cations from protein bindings in insufficiently buffered solutions. The order of concentration maintenance following one week formalin fixation in animal tissue was approximately Pt, Pb (≤10% washout) > Fe, S, C > Mn > P > Cu > Zn, Sr > Rb, Ca > Na, Cl, K, Li (≥90% washout, [27] and own

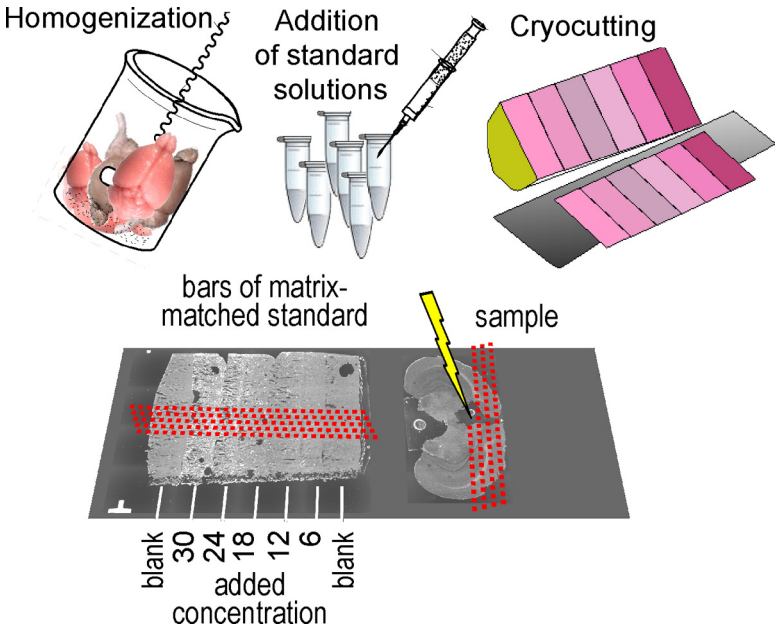

Fig. 2. Preparation of matrix matched standards and measurement procedure of first sample and afterwards standard in the same analytical run.

unpublished data). If the storage volume of formalin is sufficiently small even additional binding to cerebral white matter of Zn washed out from high concentration regions has been regularly observed. In the special case of Zn, washout and redistribution can be circumvented by precipitation as ZnS during perfusion with a buffered 1% Na_2S solution [28]. When formalin fixation is followed by immersion in 30% sucrose (common in immunohistochemistry) or dehydration in a series of increasing concentrations of alcohol for paraffin embedding a considerable shrinkage of the tissue has to be taken into account, amounting to ≈15% in either direction and to 40% in volume [29]. If referenced to the shrunken volume concentrations would be 65% too high.

2.2. Calibration

Calibration strategies in MSI by LA-ICP-MS have been the subject of a dedicated review in 2012 [30]. Here a series of new or additional aspects oriented to application are described.

2.2.1. External standards

2.2.1.1. Certified reference materials. Up to now, certified standard reference materials (SRM) for biological tissue – comprehensively reviewed in [30] – are present as lyophilized powder. To match the consistency and density of microtome sections of native biological tissue containing 70–95% water SRM have to be reconstituted with water, frozen and cryo-cut. Available are liver, bone, muscle and serum, entire fish, fish otolith, oyster, mussel and lobster powder, powder of leaves from apple, peach, tomato, spinach and pine needles. The offer is thus restricted to a few applications.

2.2.1.2. Sections of spiked tissue homogenates. Therefore, most commonly homogenates of analogous tissue were spiked with known amounts of elements of interest as illustrated in Fig. 2 and as described in some original publications [31,32]. The added concentrations are chosen within the biologically relevant range not exceeding the blank concentration by more than a factor of 10 (e.g., Mn in mouse brain is 0.5–1 $\mu g\,g^{-1}$, e.g., to mouse brain homogenates were added 0.5, 1.0, 1.5, 2.0 and 2.5 $\mu g\,g^{-1}$ of Mn) [32]. Element concentrations in standard homogenates were validated by ICP-MS analysis after microwave digestion. Standards should be placed together with the samples in the same ablation chamber and measured at least after the sample as conditions and sensitivities usually asymptotically stabilize towards the end of a measurement run. Variances in wet slice thickness of sample and standard should be corrected for. Perfect homogeneity and uniformity of dry slice thickness is not a key issue as the sample is also not homogeneous and standards should cover the range of dry thickness, granularity and micro-local concentrations found in the sample. Rather relevant seems the accuracy of average added concentrations and stability of the multi-element-homogenate suspension.

2.2.1.3. Alternative standards. Especially, when the sample material is scarce and no analogous material is available one practical alternative may be to spray or spot standard solutions directly onto small areas of a neighboring section of the sample. For the special application of hair analysis Cheajesadagul et al. [33] produced metal-spiked keratin film layers which proved superior to hair strands immersed into standard solutions.

Non-matrix matched methods have been explored such as sections of an array of frozen cylinders of spiked blood [34], sections of spiked gelatine [24], sections of spiked tissue embedding medium [35], tetra-ethyl-orthosilicate gel mixed with 10% metal-spiked tissue homogenate [36].

2.2.2. Internal standards

The use of internal standards might be amongst the topics most debated by concerned scientists. The approach chosen for a given analytical question can thus be a best compromise rather than ideal. Measured concentrations should reflect the situation in vivo as close as possible. In order to allow comparisons of groups small relative standard deviations from sample to sample and robustness are desirable.

2.2.2.1. Matrix elements as reference. In biological samples mostly ^{13}C, for selected applications also P, S or Ca have been used as internal reference for normalization of elements of interest [37–40]. Theoretical physico-chemical aspects have been extensively

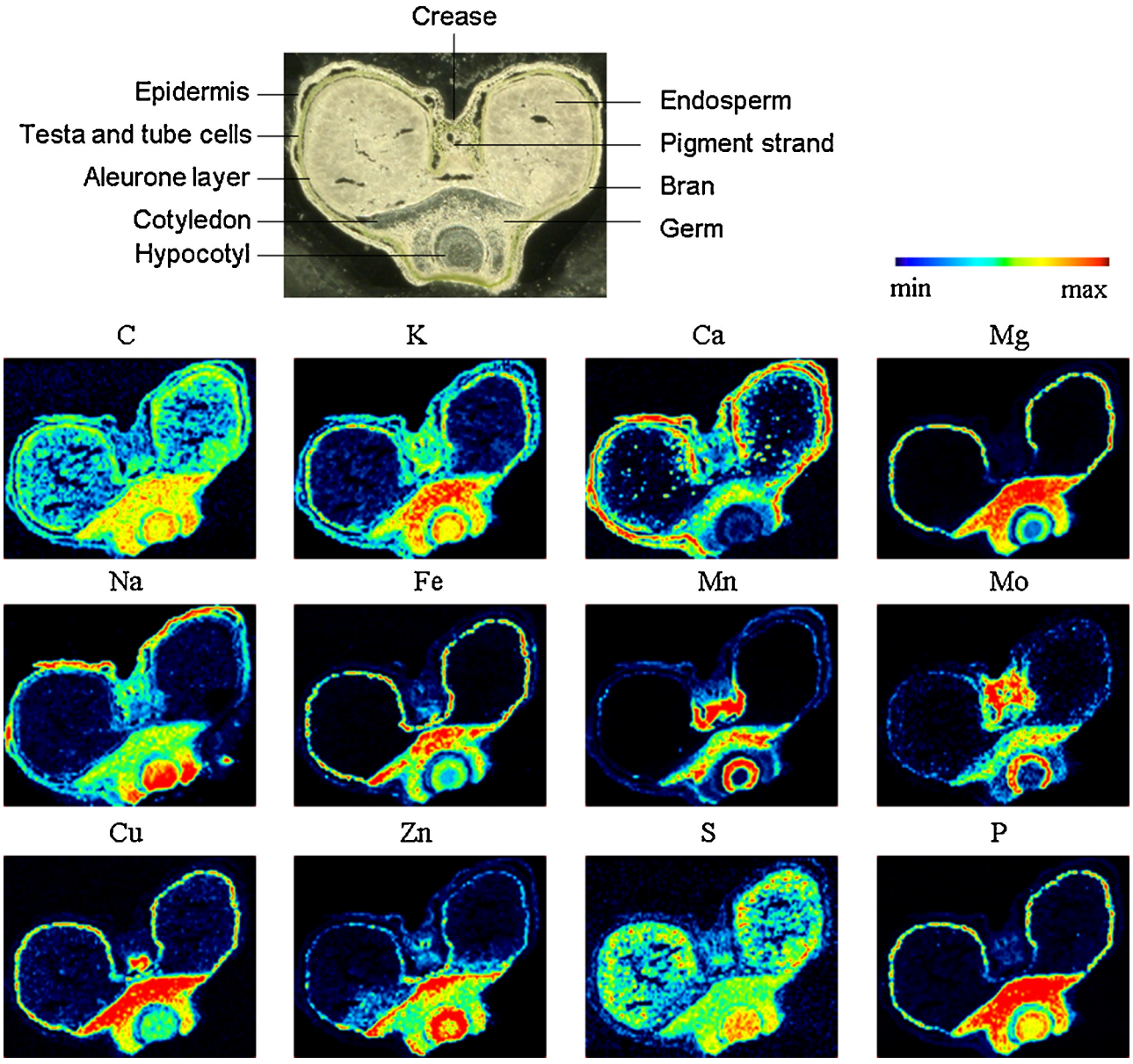

Fig. 3. Optical image of a wheat grain cross section and corresponding multielement LA-ICP-MS images scanned with a spot size of 25 μm, residual space between lines of 15 μm, a scan speed of 40 μm s^{-1} and 0.65 s acquisition time for one data point making a pixel size of 26 μm × 40 μm. The images presented here in parallel are contained in the *z*-stacks of 34 serial sections – separate for each element – given as electronic supplement of [85]. Note the distinguished accumulation in bran layers, endosperm and germ. (Dimension 3.2 mm × 2.8 mm).

discussed by Frick and Günther [41] – concluding that ^{13}C is unsuited – while in practice simple facts of image calculation and analysis prevail as in part discussed already by us [42]. Any method using pixel-wise quotients of two image files is very sensible to division by zero and noise problems. These can in part be overcome by smoothing of the divisor image. Artificial high values at edges, clefts and holes in the sample remain because of too low pixel values due to partial volume effects. Furthermore, it has to be considered that for biological questions wet weight concentrations are of most decisive interest. While cryo-cutting, the tissue has almost its original water content. A wet cryo-microtome section of e.g., 30 μm preset thickness – after mounting onto a glass slide – dries down to locally different thicknesses depending on the local water content and tissue consistency before measurement.

When normalizing per pixel to an internal standard element, concentrations become artificially low in structures with low water content and, therefore, high ^{13}C signal such as cerebral white matter (70% water) contrasting with cerebral grey matter (80% water). Therefore, normalization to ^{13}C not per pixel but to ^{13}C averaged across the entire section seems optimal to us in order to correct for variability from sample to sample in wet slice thickness and in average sensitivity. The image undergoes a simple scalar operation and there is no noisy operation between two image files. Drifts in sensitivity within an analytical run cannot be corrected by this per sample approach but anyhow could be overcome by sufficient initial cell washout and stabilizing operation conditions by many groups. In some cases opposing drifts of ^{13}C and e.g., ^{63}Cu unrelated to washout were observed, here a pixel-wise normalization to ^{13}C would introduce additional bias.

Further problems arise, when due to different thickness of the dry sample – due to different water content before drying – the width of the ablation line or the shape of the ablation crater is not constant.

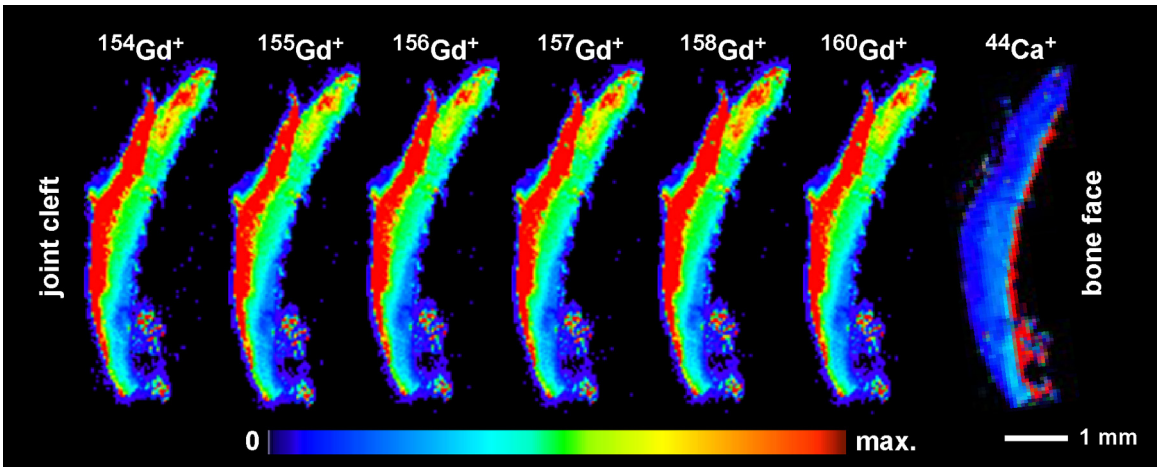

Fig. 4. LA-ICP-MS imaging of gadolinium isotopes distribution in patella articular cartilage. For simulation of human MRI arthrography conditions – where contrast agent is injected into the joint cleft to detect discontinuations of the cartilage faces and their viability – here bovine patellae were incubated for 24 h in 2 mM $[Gd(DTPA)]^{2-}$. Thereafter, pieces of cartilage where dissected and cryosectioned. Note, that there is not a step-less gradient but a clear border between a superficial and intermediate layer. In the lower part – where the sectioning plain was oblique to the layers – also the deep and the calcified layer, adjacent to the bone, can be discriminated as confirmed by the Ca image. The ablation was conducted with a spot size of 60 μm, residual space between lines 30 μm, ablation speed 60 μm s^{-1}, acquisition time per pixel 1.3 s, resulting in a pixel dimension of 77 μm × 90 μm. The maximum count rate of the scale bar is 4×10^4 for ^{154}Gd, 3×10^5 for ^{155}Gd and ^{157}Gd, 4×10^5 for ^{156}Gd, ^{158}Gd and ^{160}Gd.

Here, in the authors opinion, the best strategy to the authors seems to be is to optimize ablation conditions for complete ablation at a constant width throughout the thickness range of the sample.

The described approach applies to sections of solid tissue with constant wet thickness. For samples with variable wet thickness as e.g., entire plant leaves one can hardly renounce on a per pixel internal standard.

2.2.2.2. Solution based calibration. Introducing a second stream of a continuous aerosol produced from a calibration solution by a micro-nebulizer (e.g., ARIDUS™, Cetac [43]) into the injection tube of the ICP torch offers the possibility to control for stability of the plasma and the mass spectrometer independent from the ablation apparatus. On the other hand, if the calibration aerosol stream is not perfectly stable additional bias may be introduced and polyatomic interferences are a greater issue in wet plasma. Irrespective of the potential for correcting drifts of sensitivity when nebulizing a single element reference solution it is hardly imaginable that calibration by a series of matrix adapted external solid standards could be replaced by online addition of a dilution series of multi-element standard solutions as the latter does not control for the ablation process.

2.2.2.3. Parallel layers of coatings. Austin et al. [44] coated slides with poly-methylmethacrylate (PMMA) films which contained organometallic Y and Ru as reference elements, and Cu and Zn as added standard, prior to mounting the samples. The authors claimed that the polymer matrix was ablated in a similar fashion to the soft tissue as demonstrated by close agreement in the determined values.

In a quasi complementary fashion, Konz et al. [45] sputtered Au onto the surface of the samples yielding plausible and considerably lowly noised results. For direct comparison, this group also measured some uncoated samples mounted onto Au sputtered slides. Sputtering onto the sample surface was judged more reliable.

Given the fact that the thickness of the sample layer is not constant, for simple geometrical reasons sputtering the internal standard onto the sample seems of highest robustness and accuracy to us. In thick sample areas (compared to normative conditions) ablated incompletely this method will slightly underestimate concentrations (lower ratio of ablated sample material to ablated sputtered layer) whereas the use of substrate coating as standard risks strong overestimations. In the extreme case, at a position, where the laser focus does not reach the surface of the glass slide – may it be due to high sample thickness or to an abnormally high focus position – a measurable amount of sample but no glass coating would be ablated leading to a local division by zero problem or a local concentration value tending to infinity.

2.3. Operation and ablation modes

2.3.1. Ablation modes

Laser ablation for imaging has been performed in a true raster mode ("shot to shot"), or in line scan mode ("fire on the fly") which in turn can be continuous or come with a trigger signal at the beginning of each line. In the true raster mode [35,46] points at predefined positions are ablated, ideally equidistant in all directions and overlapping or not. This makes image reconstruction very easy, leading to undistorted images but synchronization between MS and ablation apparatus as well as removal of interposed mass spectra (data points) without sample material may be challenging. The reference voxel (smallest volume element corresponding to one data point) is slice thickness times *x*-distance times *y*-distance of raster points. At non-overlapping conditions the volume of the ablation crater which at best is available for MS-analysis makes only a fraction of the voxel volume, incomplete in *x*, *y*, and *z*, direction.

Line scans assure that every mass spectrum contains sample material and reduce bias by variability of subsequent laser craters and fractionation effects during ablation. The volume of one voxel is the product of original slice thickness, *x*-feed and *y*-feed of the *xyz* stage. Thereby *x*-feed is the product of ablation line speed and the acquisition time of a single mass spectrum, which in turn is the sum of the dwell times of measured elements. *Y*-feed corresponds to the distance between the centers of the lines. Oversampling in either direction allows voxel sizes smaller than the laser spot diameter. In Table 1, consequently, the *x*, *y* pixel dimensions are given. We chose this mode for all examples given here allowing sometimes oversampling in *x*-direction but always leaving residual space (≥20% of spot diameter) between ablated lines in order to avoid breaking, undermining and sparkling of tissue fragments. A continuous data stream challenges reconstruction, as it has to be chopped into lines, the length of which has to be determined a posteriori causing shear of the image if not performed properly [47].

The optimal solution seems the insertion of a trigger signal into the data stream at the beginning of each line or initial deposition of each line measurement as separate data file as realized by many work groups [24,40,45,48].

2.3.2. Minimization/resolution of polyatomic isobaric interferences

Isobaric interferences have been extensively dealt with in the literature on ICP-MS, here only aspects that influenced recent work on bio-imaging LA-ICP-MS are given.

2.3.2.1. Optimization of plasma composition and conditions. Several groups have been using He/Ar mixtures as carrier gas or He alone as initial ablation gas, while secondarly adding Ar to the carrier gas stream ([49], 2 volume cells, see Section 2.5). A fraction of He in the plasma can considerably reduce the formation of polyatomic ions especially of Ar species. The aerosols generated from laser ablation of dried tissue sections lead to a quasi dry plasma; polyatomic isobaric interferences are of minor concern compared to ICP-MS of nebulized solutions and usually create a tolerable constant background that can be subtracted. However, higher ion yields and up to three times higher sensitivities could be obtained in (slightly) wet plasmas for a series of elements when introducing nebulized solutions (c.f. Section 2.2.2) [43] or water/methanol [50] into the LA carrier gas stream. Sensitivity could also be improved using other additives such as methane [50]. Also geometry and shape of the plasma have been optimized for lowest production of interfering species at stable conditions and acceptable ion yields by torch and coil design (e.g., interlaced coils in the Bruker Aurora M90 [51]) and tuning of the three gas streams.

2.3.2.2. Use of the collision/reaction cell, kinetic energy discrimination. For selected analytes and applications the above mentioned measures may not be sufficient and interferences may further be suppressed by gas collision/reaction followed by extraction of ions within an appropriate range of kinetic energy. Lear et al. [52] obtained by a factor of 100 higher sensitivities for ^{56}Fe and by a factor of 10 for ^{44}Ca when using 3 mL min^{-1} of H_2 as reaction gas in order to reduce $^{40}Ar^{16}O$ and $^{12}C^{16}O_2$ in the Agilent 7500e. However, this was on expense of an at least 14 times higher signal at m/z 13 originating from $^{12}C^{1}H$ thus making normalization to ^{13}C and use for routine bio-imaging applications impossible. Furthermore a higher background at m/z 39 due to $^{38}Ar^{1}H$ occurred.

Jackson et al. operated the reaction cell at a flow of 2.5 mL min^{-1} of H_2 while detecting Se [48]. DaSilva and Arruda [53] detected Se and S as $^{80}Se^{16}O^{+}$ and $^{32}S^{16}O^{+}$ after the sample ions reacting with 0.7 L min^{-1} of O_2 in the dynamic reaction cell of the Elan DRC-e.

2.3.2.3. Mass analyzers. Sector field (SF) instruments operated at medium (e.g., 4000) or high mass resolution (e.g., 10,000) allow resolving several isobaric interferences, provide highest sensitivity and have been successfully used for LA-ICP-MS imaging by many groups (c.f. Table 1). When higher numbers of isotopes are to be monitored quadrupole or ToF [54] instruments tend to allow faster analyses than Nier Johnson SF instruments operated in peak hopping mode. Triple quadrupole ICP-MS instruments offer the possibility of filtering ions at one nominal m/z, reacting with a reaction gas and detecting the bi- or polyatomic product ions. This tandem mode enables very low detection limits for challenging elements such as e.g., As, Se but usually allows detection of only one element simultaneously.

2.4. Data treatment

Typically, the first step of data treatment involves reconstruction of a 2-dimensional image present in an image file format such as MATLAB, TIFF etc., from ASCI raw data of ion intensities. In a second step regions of interest (ROIs) are delineated obligatorily comprising the background and facultatively the entire section and anatomically defined ROIs depending on the question. Then average ion intensities are read out of ROIs. In the third step average and pixel wise ion intensities are transformed by the same scalar operation (background subtraction followed by multiplication with a calibration factor) into concentrations. In further steps calibrated images – where the pixel values are concentrations – are displayed at a selected color scale, ideally linear and starting from zero. Element images are coregistered to optical images from the same section taken before ablation, registered to neighboring sections and combined to 3D-datasets, or overlays of several elements or modalities are created.

For this purposes hand-written MATLAB routines (Mathworks, Natick, MA) [53,55,56], Origin (Originlab Corporations, Northampton) [57], or the in-house written C++ software IMAGENA [47] and further handling by Pmod (Zurich, Switzerland) [32] or the Python program ISIDAS in conjunction with Maya Vi2 (Enthought Inc.) [40] or the SMAK-package [48] have been used.

2.5. Improvement of spatial resolution

In any spatially resolved analytical technique the concentration limit of detection is inversely related to the size of the smallest analytical volume element (voxel). Therefore, in MSI by LA-ICP-MS the spatial resolution that can be realized by lowering the spot-size is limited by the concentration of the analyte and the smallest amount of analyte that needs to be ablated to allow detection in one cycle (e.g., 50 fg of Pt as indicated in [58]). The latter depends on the sensitivity of the ICP-MS and on the transport efficiency for ablated aerosols.

Thus, the precondition for improving spatial resolution is a sensitive ICP-MS and measures include improving transport efficiency by minimizing death volumina, wash-out times and aerosol dispersion at the one hand and at the other hand providing smaller spot sizes.

Smaller spot sizes in turn challenge the stability of vertical focus position and may require a precise compensation of focus drift (tilt correction using a frame of focus reference points).

Practically the size of the area to be scanned (the field of view) also limits the spatial resolution at which it can be imaged (x, y, pixel dimensions) as total analysis time, stability of the ICP-MS over e.g., more than 12 h, Ar/He consume and volume of the generated data are not illimited.

2.5.1. Commercial ablation systems

In routine applications of MSI by LA-ICP-MS spatial resolutions, for instance, of 60 μm in mouse brain and of 200 μm in plant leaves and human brain sections proved as reasonable to handle, providing sufficient stability and sensitivity while the necessary morphological details such as anatomical layers could be resolved.

For chemical analysis of smaller-sized structures such as single cells, kidney tubules, liver lobules, nervous system of insects, cross sections of plant roots etc., sensitive analytical techniques with much higher spatial resolution down to the low-micrometer and even nanometer ranges are required. Here, commercially available ablation systems have considerably improved in recent years in terms of laser conditions, size, shape and homogeneity of the laser spot, cell washout behavior and transport efficiency of the ablated material. For example, the Cetac LSX 200Plus launched in 2001 allowed 10 μm as smallest spotsize, the UP213 launched before 2005, the NWR213, launched about 2009, Applied Spectra J100Series (of 2010), Coherent GeoLasPro (of 2008), and Cetac LSX213 G2+ allow 4 μm.

A fast washout behavior of ablation cells considerably contributes to sensitivity and minimization of signal dispersion from pixel

to pixel. It has been improved by capturing the aerosol stream from the sample by a laser transparent small volume outlet cup centered onto the laser focus and sitting almost flush with the sample surface such as in the NWR213 or further by the 2 volume cells such as the HelEx™ design realized in the Cetac/Photon machines Analyte G2 assuring a washout to <0.3% signal per second.

Ablations in He stream can be considerably cleaner with less non transported material sparkles deposited on the surrounding sample surface compared to ablations in Ar stream [59]. High speed movies of single shot ablations in quiescent atmosphere evidenced a fine filiform vertical expansion of aerosols produced in He while aerosols in Ar spread rather horizontally very close to the sample surface [60]. Ablations in He stream and secondary addition of Ar to the carrier gas stream is assured in 2 volume cells such as HelEx™ or the MMG Sample cell provided by Coherent in conjunction with the GeoLasPro optical system.

Meanwhile, several ablation systems allow spot sizes of 1 μm, the NWRfemto, launched in 2012, in its standard configuration, others when equipped with a custom aperture such as the Cetac/Photon machines Analyte G2 (standard 2–3 μm) and the New Wave UP193FX both equipped with the same ATL Ex300Si <4 ns ArF eximer laser or the Applied Spectra J200 equipped with a frequency tripled 343 nm amplitude S-puls Yb-fiber femtosecond laser (standard 3 μm). Improvements in spot homogeneity and rectangular spots allow also to reach 1 μm resolution by oversampling e.g., 3 μm spots.

The examples of Figs. 1, 3 and 4 and Figs. S4 and S5 were obtained using a New Wave NWR213 (Fremont, CA, USA) ablation system equipped with a solid state Nd:YAG laser (wavelength 213 nm) and a 10 cm × 10 cm ablation chamber coupled to a quadrupole (XSeries 2, Thermo Scientific, Bremen, Germany) or to a double focusing sector field ICP-MS (Element 2, Thermo Scientific) for our last experiments including the examples given here.

Further options and degrees of freedom for bio-imaging arose from the introduction of large format cells (e.g., 15 × 15 cm^2) and cryogenic cells. When brittle material with low adhesion to the substrate is to be ablated, such as dried plant leaves [61], splintering of fragments can be considerably reduced by ablation in frozen hydrated state in cryogenic cells. Furthermore, in frozen hydrated material depth profiling is feasible [62] and artificial translocation of highly mobile species such as alkali cations during drying can be avoided.

2.5.2. LMD-LA-ICP-MS

A second strategy for increasing spatial resolution commenced before the emergence of commercial ablation systems providing sub 4 μm resolutions consisted in coupling a dedicated laser microdissection apparatus (LMD) to a sensitive ICP-MS (German patent WO2010115394 A1 granted Dec. 2010). LMD was originally designed for isolation of specific areas or cells of interest out of a tissue section for further studies. In LMD-ICP-MS, the LMD apparatus (here mmiSmartCut Plus, Molecular Machines and Industries, Zurich, Switzerland) works as ablation system for the ICP-MS. The LMD was equipped with a Nd:YAG laser with a pulse energy of 110 μJ at 355 nm wavelength (repetition rate 100 Hz and pulse duration 1.5 ns) to provide a highly focused beam with a spot size down to 1 μm and below. Small bottom-opened ablation chambers of different designs were constructed and tested. The glass slide bearing the sample was placed and tightened below. Of these a cylindric cell of 1 cm^3 volume enabled washout to background level within 0.6 s and was used for further studies [63].

The laser beam came from the bottom through the glass substrate and was focused on the sample surface. Spot sizes of 4 μm and 2.5 μm were used to ablate 10 μm native mouse brain cryo-sections (Figs. S1, S2B) and 10 μm sections of a wheat root (Fig S3), respectively. Note that 10 μm are the thickness of the wet section preset at the microtome which dries down to 3–4 μm. The scan speed was properly chosen considering the acquisition time of the ICP-MS, so that the product of both making the lateral *x*-resolution matched the laser spot size. The tissue was fully ablated, while no glass substrate was ablated. The ablated material was transported by Ar as a carrier gas to the ICP source of either the quadrupole XSeries 2 or the sector field Element2 instrument, respectively, where it was ionized and the ion intensities of the analytes $^{56}Fe^+$ and $^{64}Zn^+$ or $^{158}Gd^+$, $^{232}Th^+$, $^{238}U^+$ (hippocampus in the mouse brain) or $^{24}Mg^+$ and $^{31}P^+$ (in wheat root) were detected. Furthermore, $^{23}Na^+$, $^{24}Mg^+$, $^{31}P^+$, $^{39}K^+$, $^{56}Fe^+$ and $^{64}Zn^+$ could be resolved at 6 μm.

In comparison, using the NWR213 and 4 μm spot-size, while quadrupole ICP-MS and 10 μm brain sample were the same, not sufficient signal was yielded for imaging although ablation was complete. The smallest practicable spot size here was 10 μm. This suggests that eventual advantages in aerosol expansion and transport efficiency could be obtained with the LMD-setup. The respective pictures exemplify the capabilities of this technique to image fine layers of down to 20 μm width in a concentration range of 5–50 μg g^{-1}. Fig. S1 shows Fe, Zn and P images of the hippocampus and allows clear and sharp discrimination of the layering and segment pattern. Fig. S2B shows the identical area in a neighboring section which had been incubated in a solution containing 100 μg g^{-1} Gd and U and 10 μg g^{-1} Th in order to study their binding. Fig. S3 shows LMD-ICP-MS images of Mg and P in a cross section of a wheat root. Compared to cortex, much higher Mg and P were found in stele, mainly in endodermis and pericycle, followed by phloem. The epidermis of the root also showed enrichment of Mg and P, in agreement with other studies.

2.5.3. Other approaches for improving spatial resolution

Günther and coworkers engineered an ablation cell with a tube geometry and confluent design optimizing the transport of ablated material in order to minimize dispersion. Only a partial stream of 0.6 L min^{-1} He was conducted over the sample with minimal dead volume. This flows into a larger argon carrier stream of 1.1 L min^{-1} leading into the plasma. A modified GeoLas C ablation system equipped with an ArF eximer laser allowed spot sizes of 1 μm and sensitivities of 0.01 μg g^{-1} for diverse lanthanide isotopes [49]. Tissue sections labeled by up to 32 antibodies tagged with 32 different lanthanides or isotopically enriched lanthanide tracers, respectively, were mapped at 1 μm resolution [54] using a CyTOF ICP-ToF-MS instrument demonstrating unique multiplex capabilities.

Tip-enhanced near-field LA-ICP-MS, by means of a thin Ag needle, allows ablation of sample surfaces at sub-μm and nm scale. Radiation intensity singularities are formed when a very small conductive object is immersed in the light radiation field. Ablation of an 300 nm × 300 nm area at a thickness of 20 nm of an Au layer corresponding to 0.5 fmol Au yielded a signal of 9000 cps [72,73]. However, the step from point ablation to reproducible line scans and imaging has not yet been undertaken.

3. Applications of LA-ICP-MS bio-imaging – 10 years of work

3.1. Element-architecture in healthy organisms

3.1.1. Animal tissue

In 2003 the group of J. Feldmann in Aberdeen presented an isoconcentration profile map of Cu in sheep liver obtained by a LA-ICP-ToF-MS raster scan which was the overture of a since then precipitating success story [1]. Jackson et al. in Dartmouth college (NH, USA) presented in 2006 the first LA-ICP-MS images of Fe, Cu,

Zn in a native coronal section of an entire rodent brain hemisphere revealing its physiological metalloarchitecture [26].

Since then, brain sections in several cutting directions at many positions from healthy control mice and rats of several ages have been mapped by LA-ICP-MS by others [23,30,31,34,37,38,64–66] and us [2,22,32,43,65,67–73]. For illustration we present MSI by LA-ICP-MS of C, P, Mn, Fe, Cu, Zn in parallel with a block face incident light image obtained before cutting this very horizontal native rat brain section and a transmitted light image of the section after mounting onto the slide before ablation (Fig S4). The section had been embedded in blue freeze cutting medium for better optical contrast.

A spatial impression of characteristic structures is given by regarding coronal, saggital and horizontal native sections of three different control brains in parallel as given in Fig. S5 for Fe, Mn and the optical image. The widespread Watson and Paxinos Atlas of the mouse and rat brain allows identification of innumerable details in these canonical planes [74]. Further anatomical information and correlation with many gene expression profiles in rodent brain is provided by the Allen Institute database (http://www.alleninstitute.org). Furthermore, we imaged native rodent heart [65], kidney [55] and spinal cord [75].

3.1.2. Human biopsy/autopsy tissue

Single or few specimens from appendix [76], oviduct [76], breast [77], lymph node [76,78], stomach [77], brain [68,79–81], chamber angle [45] and lens [62] of the eye were investigated. Mostly the focus was on prove of principle and technical issues and the material formalin fixed so that due to leaching of most metals only limited conclusions with respect to physiology were possible.

3.1.3. Plants

Element imaging techniques have contributed to understanding the functional anatomy throughout roots, stem, leaves where capillary bundles and layers assure longitudinal and selective transversal transport. S could be localized to the edges of sunflower leaves [53]. In leaves of tobacco grown on nutrient rich standard soil Mg, Mn, Fe, Cu, Zn were enriched in the xylem of the leaf veins and of shoots, while Pb and to a certain extend also Zn were sequestered to the edges and apex of the leafs [82]. In the leaves of *Elsholtzia splendens* Mg, P, K, Mn were enriched in the leaf veins while S and B were more evenly or latero-apically distributed [83].

Especially in seeds the element distribution throughout specialized organs and layers is highly differentiated. LA-ICP-MS images of sections through seeds are published for the seashore mallow with beautiful pentagonal fruits (Ca, Zn, K, Na) [96] , the peanut [84] and wheat [85]. Here we illustrate multielement images of a section of the same wheat seed as in [85] at a plane in between those shown in the body of [85] (Fig. 3). Consistently, in the wheat seed and the peanut, it turned out that all nutrient elements were enriched in the germ, while the starchy endosperm was poor in all nutrients. In wheat the germ is usually removed in the milling process because it contains lipid that limit the keeping qualities of flour. More in detail, Mo was highly selectively enriched in the radicle (= root primordia, only in the paired lateral parts in wheat) of the embryo and in the main vascular bundle (in the fold opposite the embryo). Mo as a cofactor of nitrate reductase is essential for nitrogen fixation in soil bacteria such as *Azotobacter* – known since 1930 [86] – and [84], the root primordia apport here a starting amount of Mo to enable optimal azobacterial growth in their surroundings. Furthermore, Fe and Cu occurred at high levels in the coleoptil (protective sheath covering the emerging shoot) K, Mn, P, Mg in the scutellum, Mn, Cu, B in addition in the nuclear projection, Ba and Sr in the outer part of the scutellum and Ca in the aleuron sheath of the starchy endosperm. A similar distribution of Fe was observed by Singh and coworkers using μXRF, μPIXE and μXANES [87], speciation pointed to Fe–O–P–R and Fe–O–S–R coordination of Fe.

3.1.4. Non-vertebrates

Sections of bees [56], slugs [88], water fleas (daphnia) [18,89], amphipoda [48] have been imaged by LA-ICP-MS revealing much details about the functional anatomy that have been almost unknown so far. Lacks of knowledge even spread to the optical level as entomologists rarely access microtome laboratories. As these animals all use haemocyanine the Cu images give an immediate orientation on the distribution of blood.

3.2. Tissue at pathological conditions

3.2.1. Biopsy/autopsy specimens

Native cryo-sections of fibrotic/cirrhotic and control human livers were subject of a recent own study [90]. The elemental images showed in normal liver the regular lobular organization with higher Fe at the rims of lobules and enrichments of Cu and Zn in the centers of some lobules. In fibrotic livers the gross of metal content was concentrated to the residual islands/nodules of functional tissue while the fibrotic septae around contained little metal. LA-ICP-MS imaging allows measuring the metal content as additional parameter in cryo-sections from routine biopsy samples when the amount of material is too small for ICP-MS of acidic digests.

Furthermore human specimens of melanoma invaded lymph nodes [78], arthritic knee cartilage with $Ca_3(PO_4)_2$ crystals[91], breast tumor [77], stomach [77], oesophageal tumor [76] were analyzed.

3.2.2. Experimentally induced disease

MSI by LA-ICP-MS is especially attractive and can bring its strength into play, when in the same individual a lesioned and a healthy side of a paired symmetric structure – such as the two brain hemispheres – can be compared or pathological – such as cancerous – beneath unaffected tissue. MSI by LA-ICP-MS can considerably contribute to characterization and validation of disease models in comparison to naturally occurring pathological cases and to the understanding of the underlying pathophysiology.

Element distribution around tree bark wounds of different age was studied by Siebold et al. An enrichment of Mg and P in the transitional growth zone was found [92].

In a 2008 science paper the teams of Feldmann and Scar evidenced excess Zn and Mn in liver abscesses of transgenic mice lacking the endogenous bactericide chelator S100A8/9 calprotectin using imaging and ICP-MS analysis of laser micro-dissections [93].

A series of studies assessed rodent models of Parkinson's disease [22,23,32,38], furthermore Alzheimer [70], tumor [68] and stroke models [68] were studied.

3.3. Organisms after exposition to metal/hetero-element compounds at lifetime

3.3.1. Hyper- and hypo-accumulating plants

Plant accumulating Hg, Cd, Pb etc., are of key interest for the restoration of contaminated soils. Ni enrichment in root cross sections of an aster flower species known to be an effective hyperaccumulator was mapped in the Prohaska group in Vienna [94]. An active sequestration mechanism of Pb and Sb was observed in root compared to stem and frond cross sections of fern naturally occurring at a contaminated area [95]. Han et al. [96] studied the suitability of a salt tolerant malva for accumulation of Zn, and detected a high enrichment in the seed embryo but only when the offer of NaCl was low. In the Cu tolerant *Elsholtzia splendens* transport of Cu via the leave veins to the edge of the leaf could be detected in young leaves whereas in older leaves the

apical portion was preferentially Cu rich [83]. Cd and Zn enrichment in the leaves of *zygophyllum fabago* was studied in a multimodal approach involving LA-ICP-MS, ICP-MS, PIXE, X-ray absorption fine structure and biochemical analyses [21]. In a cross section of Indian mustard stem Cd and nutrient elements were studied [97].

Maize in turn had a high resistance against Hg, whereby the root endodermal barrier proved almost impermeable for Hg^{2+} [35]. Se showed a homogeneous distribution in the leaves when sunflowers were irrigated for 29–45 days with Na_2SeO_3 [53].

3.3.2. Development of drugs, therapeutic nanoparticles, contrast agents and their delivery

A study by Pugh et al. [65] imaged Gd and Pt after local co-infusion of Gd labeled lipid nanoparticles and carboplatin at 6, 24 and 48 h in one rat (vs. 1 control) each and in 2 pigs (vs. 1 control). As intended with this method termed "convection enhanced delivery", designed for treatment of brain tumors, a quite homogeneous dispersion of the drug over a comparably large volume, ≈20 mm diameter in the pig and ≈1.5 mm in the rat brain, corresponding to 1/5 and 1/10 of the brain width, respectively, was obtained. The border between gross anatomical compartments was respected. In contrast to LA-ICP-MS the MRI could not differentiate between bleeding and Gd enrichment. See Section 3.5. for a larger analogous study. The same group studied in one mouse vs. one control the disposition of Gd tagged liposomal nanoparticles in tumor and kidney after local injection into an experimental subcutaneous tumor [25]. See Section 3.6. for the subsequent large scale studies.

The group of U. Karst in Münster recently presented a body of work measuring Pt 1 h and 48 h p.i. in the critical organs testis, kidney and cochlea (this minuscule structure with air, soft matter and bone components necessitates highly demanding embedding and cutting procedure) of mouse [98] and after repeated chronic application followed by a washout phase in mouse [98,99] and human [76] tissue. In contrast to our previous images of native fresh frozen kidney sections 0.5 h p.i. where total bound and unbound Pt accounted for the measured signal, in this 1 h p.i. image the unbound fraction had been washed out by the fixation procedure revealing bound Pt in the cortical proximal tubulus compartment.

The tubular distribution of Pt in rodent kidney after a single dose of cisplatin and 5 days washout was also evidenced at high resolution by Moreno-Gordaliza et al. [58]. The team of C. F. Wang in Taiwan accomplished a series of works on the disposition of different contrast agents in mice organs [100,101].

Au and Ag tagged nanoparticles could recently imaged even in single cultured cells [102]. The fate of nanoparticles in the environment and alimentary chain also in view of identifying indicator species for environmental monitoring has been the subject of two studies. Bioaccumulation of Cd in form of CdSe/ZnS quantum dot nanoparticles in freshwater shrimp (amphipoda) was considerably higher than of free Cd^{2+} [48]. Anionically functionalized Au nanoparticles showed higher translocation to rice shoots than did Au particles with neutral and cationic derivatives [39].

The distribution of the new Br containing drug compound TMC207 was studied in longitudinal whole body sections of rats 1, 4, and 8 h after application by Izmer et al. [103]. Here, MSI by LA-ICP-MS is a highly valuable tool in drug development complementing and adding to the wide spread technique of autoradiography of whole body sections after injection of the [^{14}C] radiolabeled candidate compounds.

3.3.3. Stable isotope tracer studies

Urgast, Feldmann et al. injected a ^{70}Zn enriched tracer into rats (one animal per condition and 2 controls) 14 or 7 days before victimization followed by a second injection of a ^{67}Zn tracer 1 or 2 days before victimization at doses 5 or 15 μg. They observed that an about 3 fold fraction of Zn is exchangeable within 1–2 days in the liver and a 2-fold fraction in aorta wall compared to muscle tissue [24]. The Zn uptake in the water flea (Daphnia) was studied using a ^{64}Zn enriched tracer [89] evidencing high exchangeability in gut, gills and eye and low Zn turnover in the eggs.

3.3.4. Other

Feldmann et al. explored the migration of Sn, Pb, Bi from shotgun pellets in the hindlimbs of rats [104]. In lung parenchyma and lymph node biopsy tissue of former nuclear workers, deposits of U, Th and Pu could be detected [105]. The release of metals into tissue from an Ag coated Ti-V-alloy implant was studied using LA-ICP-MS and XRF [19].

In sea snails collected from contaminated areas, a preferential and almost exclusive enrichment of Hg, Pb, Cd in the digestive gland was detected [106].

3.4. Ex vivo binding/staining including immunhistochemistry

3.4.1. Immunhistochemistry/histological stains

3.4.1.1. Metal tagged antibodies/metal tagged streptavidin. Secondary antibodies tagged with a series of lanthanides are an attractive alternative for fluorescence labeled antibodies due to the multiplex capabilities and high concentration dynamical range of LA-ICP-MS. Gold and silver cluster tagged antibodies are in use for electron microscopy since a long time. Furthermore, many immune detection systems use biotinylated secondary antibodies and a streptavidin derivative that highly specifically binds biotin, as third partner. The streptavidin in turn had been labeled by a fluorochrome, an enzyme catalyzing a chromogenic reaction (alkaline phosphatase or peroxidase) or a heavy metal. Hutchinson, McLeod et al. detected beta-amyloid via immunohistochemistry using Eu-tagged strepavidin and MSI by LA-ICP-MS in their proof of principle work [46].

The group of Günter analyzed a breast tumor section labeled with a Ho tagged primary antibody directed against the breast tumor antigen HER2 [49], c.f. Section 2.5.3. Seuma, McLeod et al. used Au tagged secondary antibodies that in a next step catalyzed the reduction and precipitation of Ag and imaged Ag and Au [77]. The Jakubowski team mapped three different Ho, Tb and Tm, respectively, tagged antibodies at the same breast cancer tissue section [107].

3.4.1.2. Metals for enhancement/shift of chromogenic indicator reactions. Horesradish peroxidase coupled to secondary antibodies or streptavidin converts the chromogenic substrate diaminobenzidine (DAB) to a brown precipitate. In the presence of Ni a black and in the presence of Co a blue insoluble complex is formed. Sequential incubations and applications with washing allow to create bi-color specimens. The Ni precipitate was used by Hutchinson, McLeod et al. [46] for validation and proof of principle of MSI by LA-ICP-MS displaying perfect congruency to the optical image and potentially higher concentration dynamical range.

3.4.1.3. Histological stains. The Br and Al contained as heteroatomic or chelated constituents in the histological routine dyes eosine and haeme-alaun, respectively, were used to validate first MSI by LA-ICP-MS which provided excellent artifact free and high resolution image quality in perfect congruency to the optical image [76] and second the simultaneous connection of APCI-Orbitrap-MS and an ICP-MS to the same laser ablation apparatus [99].

3.4.2. Ex vivo binding studies of element species of interest

3.4.2.1. Binding of heavy metal cations to brain section. MSI by LA-ICP-MS was employed to identify critical compartments in biological tissue with high affinity for given heavy metal species in the frame of toxicology studies.

First binding experiments on rat brain post-mortem tissues in an aqueous solution of either uranium or neodymium (100 $\mu g\,g^{-1}$, incubation for 3 h) were performed by Becker et al. [67]. This study showed a predilection of uranyl for neuronal white matter, thus confirming its known myelinotoxic potential. Analogous binding studies with mixtures of a series of toxins of interest allow a rapid orientating evaluation of entire classes of toxins.

Such a multi-toxin binding screening study was exemplified recently by incubating a native rat brain section (30 μm) for 2 h in an aqueous solution containing the aquoions of $[UO_2]^{2+}$, Gd^{3+} and Th^{x+} (U and Gd 100 $\mu g\ g^{-1}$; Th 10 $\mu g\,g^{-1}$). The distribution of the three gadolinium isotopes measured at m/z 156, 157 and 158 (with natural isotope abundances of 20.5, 15.6 and 24.8%, respectively), is illustrated in Fig. S2A. All three isotopes show identical ion images of Gd with enrichment of the doped rare earth element in white matter (corpus callosum and internal capsule) and low binding in gray matter (e.g., cortex and hippocampus).

3.4.2.2. Element counterstain of cellular substructures. Another application of external addition of elements post mortem is specific staining of given cellular structures. Giesen et al. [108] proposed iodine (applied within a short incubation of 60 s) as an elemental dye for the nuclei of fibroblast cells that can than be detected by LA-ICP-MS. This could serve as a counter-stain for co-localization with heavy metals or particles applied at lifetime.

3.4.2.3. Penetration of Gd contrast agent into cartilage. Recently, Sussulini et al. [109] described quantitative LA-ICP-MS imaging of Gd in bovine patella cartilage which had been sectioned after incubation of the intact patellae in an aqueous solution of 2.0 $mmol\,L^{-1}$ [Gd(diethylen-tetramine-pentaacetate)]$^{2-}$. The tissue concentrations of Gd confirmed that the layering pattern observed in MRI was not a bone artefact but truly reflected Gd concentrations. Fig. 4 shows the congruent distribution of six stable gadolinium isotopes measured.

3.5. Various cases

3.5.1. Teeth

In contrast to soft tissue, in this solid and highly compact structure no drying and no shrinkage during drying occurs, therefore, the pixelwise use of a reference element – regularly Ca – is of ease, without any division by zero and partial volume problem. MSI by LA-ICP-MS of teeth grindings has been perfected [110] in a very fruitful cooperation with dentists crowned by the recent nature publication [40]. During the time period of ongoing calcification – in the definitive first molar from some days pre birth to 10 years, in the third molar from about 8 up to 25 years of age – teeth report the course of metal exposition similar to the annual growth rings in trees but with a temporal resolution of 8 days or better. Earlier, teeth had already been acceded by line scans in Amherst [111].

3.5.2. Leaves, co-planar

Although for e.g., tobacco leaves it is possible to produce co-planar cryo-sections [82], it is almost impossible to provide samples of continuous constant wet material thickness. Regularly, lateral transport and disposition of elements from the leaf stalk through the leaf veins to the leaf parenchyma and the apex is in question. Therefore intact leaves have to be mounted onto a support and laser ablated [69]. Here, MSI by LA-ICP-MS taken alone allows only referencing to dry weight as reflected by the ^{13}C signal. For a proper determination of the wet volume complementary light microscopic techniques are warranted such as optical coherence or confocal laser scanning tomography or white light interferometry.

3.5.3. Root blots of plants during growth

In a collaboration of the Prohaska group in Vienna [112], plants were grown in a box with removable walls called rhizotron. To place a blotting gel, the box was laid flat with the plant stem horizontal, one wall was removed, the soil package with the small roots growing parallel to the wall was covered first by a 10 μm permeable membrane and than by a 0.6 mm thick gel with fixating capability for the analytes of interest, here a ferrihydrid gel to fix phosphate, finally the wall was reinserted. After the desired interval the gel was removed. Element maps of dried gels reflect element uptake of the roots as well as element excretions of root apices.

3.6. Larger numbers of serial samples/group comparisons and kinetics

When performing group comparisons e.g., treated versus control subjects a high precision in the sense of low cv is paramount. Realistic are cv in the range of 10–20%. Just to give an impression, in the simple case of comparison of two independent groups and normal distribution the minimum size of each group is $n = 5$ for a cv of 10%, $n = 9$ for a cv of 15% and $n = 14$ for a cv of 20% to detect a significant group difference of 30% with 95% probability. For within group comparisons – e.g., diseased and healthy region in the same sample – the respective sample sizes would be $n = 4$, $n = 6$ and $n = 9$ (determined using the software G-Power 3.1, free download).

We obtained considerable improvements in cv when correcting for the variable slice thickness of microtome sections by normalizing sample and standard measurement to the ^{13}C averaged across the entire measurement [22]. Furthermore it is highly recommended to nest samples of the intervention and the control group because operation conditions tend to vary from week to week. All of the 7 studies described subsequently were sufficiently powered to detect significant differences between groups or between different regions within groups.

Only a few group comparisons with MSI by LA-ICP-MS were published. Austin, Doble et al. analyzed Ba/Ca ratios in longitudinal sections of decidual teeth of 25 children. They compared zones of dentin and enamel that had grown during the developmental periods before birth, during breast feeding, and during formula nutrition. Furthermore, teeth of five macaques were analyzed [40].

Recently the same research group [67] compared brain sections of 5 common mice after 8 weeks of intermittent hypoxyia versus 6 controls. The elevation of ^{59}Co from 62 to 5600 $ng\,g^{-1}$ localized to white matter, seems biologically highly non-plausible and may rather originate from a different batch (storage in metallic vessels) of formalin solution used for perfusion and fixation (here the binding or redistribution of di- or trivalent larger cations to white matter is a well known phenomenon, c.f. [26,67] and Fig. S2A) or from isobaric interferences at $m/z = 59$ may it be $^{40}Ar^{18}O^{1}H^{+}$ or $^{28}Si^{31}P^{+}$ resulting from ablating glass under the sections of the treated group. The white matter distribution pattern of O and P, respectively, is well known. We observed a congruent white matter pattern also at m/z 52 which we interpreted as $^{12}C^{40}Ar^{+}$and not as ^{52}Cr.

The group of C. McLeod and J. Bunch quantified Pt at different time points after local very slow in vivo injection of carboplatin into the brain. MSI by LA-ICP-MS of 22 rats (2 or 3 at 8 time points) that had received a dose of 75 ng could be exploited [64]. The

delivery of DNA packaged into receptor targeted nanocomplexes labeled with a fluorochrome and with Gd after instillation into the brain was assessed [66] in comparison to optical and MRI detection. Four formulations, two time points and 4 rats each making a total of 32 were studied by LA-ICP-MS.

Barst, Verbeck et al. compared Hg and Se accumulation in normal liver parenchyma and in pathologic liver macrophage aggregates in 7 fishes collected from a Hg contaminated lake [113]. Konz et al. [45] analyzed section through the chamber angle of the eyes of ten humans, but only qualitatively, and visually stated similarities in the distribution pattern with individual variabilities.

We compared Fe, Cu, Zn and Mn averaged in each of a series of brain regions of mice 2 h ($n=4$), 7 days ($n=5$) and 28 days ($n=4$) after MPTP intoxication and controls ($n=5$). MPTP intoxication is broadly used as a model of Parkinson's disease [22]. Next 18 mice 42 days after unilateral 6-OHDA lesion of the medial forebrain bundle were studied of which 12 had received L-DOPA and the other 6 vehicle [71].

3.7. Atlas approaches/3D reconstruction of serial sections

3.7.1. Atlas of formalin fixed mouse brain

In 2012 Hare, Doble et al. presented an atlas composed of 44 serial 30 μm thick coronal sections spaced at distances of 150 μm throughout the rostral 4/5 of a mouse brain that had been immersed in formalin overnight and in 30% sucrose for 3 days. Thereby sections 1–22 were mounted on a first slide, sections 23–34 onto a second and sections 37–44 onto a third slide. All sections from one slide where ablated together in a single run, which further comprised three measurements of a standard series, with a non-specified number of line-scans at non specified time points. Therefore, in the series of resulting concentration maps discontinuations between the three slides are clearly discernable. At the edges of the sections displayed concentrations are artificially high due pixel wise division by the unsmoothed ^{13}C image exhibiting low pixel values at the edges due to partial volume effects. Although the 3D reconstruction was not convincing, this work enables a comprehensive understanding of the architecture of Fe and Cu throughout the mouse brain – Zn had obviously been partially washed out – and deserves online accessibility.

3.7.2. Wheat grain germ atlas

Native 26 μm cryo-sections of the upper third of a wheat grain were produced and every other section discarded leaving 34 sections for MSI by LA-ICP-MS (c.f. Section 3.1.3., Fig. 3 and [85]). Element images were coregistered, x- and y-scaled to the optical images, then registered to each other and finally borders were added to give the same pixel dimensions (400×300) all these operations were conducted manually using Pmod 3.1 (Pmod, Zurich, Switzerland). The respective z-stack datasets were published as electronic supplement in [85]. It showed that the element images were highly consistent and artifact free. Viewing the 3D dataset in orthogonal planes through the cutting cursor position enabled unequivocal identification of anatomical structures.

4. Conclusions

The performance of MSI by LA-ICP-MS in terms of spatial resolution, quantitation, speed, robustness and stability could progressively be improved in the recent years. Commercial systems provide spatial resolutions down to the range of 2–5 μm which is the limit of appropriateness for imaging native biological tissues. However, for studying the multiple biomedical applications of nanoparticles even higher resolution would make sense. Several dozens of prove of concept and feasibility studies opened the way for innumerable upcoming applications. First applications of MSI by LA-ICP-MS for the assessment of larger groups of test organisms and group comparisons and kinetic series have been undertaken. Also the first atlas works are under way which provide comprehensive insight into the element architecture of entire organs or organisms.

Acknowledgements

The authors would like to acknowledge Thermo Scientific (Bremen, Germany) and Deutsche Forschungsgemeinschaft (DFG grant number BE 2649/5-1) for instrumental support of the BrainMet laboratory. Special thanks are given to A.M. Oros-Peusquens (Institute of Neuroscience and Medicine, Jülich, Forschungszentrum Jülich, Germany) and W. Weschke (Leibniz Institute of Plant Genetics and Crop Plant Research, Gatersleben) for providing rat brains and wheat grains, respectively.

Appendix A. Supplementary data

Supplementary data associated with this article can be found, in the online version, at http://dx.doi.org/10.1016/j.aca.2014.04.048.

References

[1] A. Kindness, C.N. Sekaran, J. Feldmann, Two-dimensional mapping of copper and zinc in liver sections by laser ablation-inductively coupled plasma mass spectrometry, Clinical Chemistry 49 (2003) 1916–1923.
[2] J.S. Becker, Imaging of metals in biological tissue by laser ablation inductively coupled plasma mass spectrometry (LA-ICP-MS): state of the art and future developments, Journal of Mass Spectrometry 48 (2013) 255–268.
[3] B. Wu, J.S. Becker, Imaging techniques for elements and element species in plant science, Metallomics 4 (2012) 403–416.
[4] E. Lombi, K.G. Scheckel, I.M. Kempson, In situ analysis of metal(loid)s in plants: state of the art and artefacts, Environmental and Experimental Botany 72 (2011) 3–17.
[5] A.J. Managh, S.L. Edwards, A. Bushell, K.J. Wood, E.K. Geissler, J.A. Hutchinson, R.W. Hutchinson, H.J. Reid, B. Sharp, Single cell tracking of gadolinium labelled CD4+ T cells by laser ablation inductively coupled plasma mass spectrometry (LA-ICP-MS), Analytical Chemistry 85 (2013) 10627–10634.
[6] C. Stadlbauer, T. Prohaska, C. Reiter, A. Knaus, G. Stingeder, Time-resolved monitoring of heavy-metal intoxication in single hair by laser ablation ICP-DRCMS, Analytical and Bioanalytical Chemistry 383 (2005) 500–508.
[7] L. Waentig, S. Techritz, N. Jakubowski, P.H. Roos, A multi-parametric microarray for protein profiling: simultaneous analysis of 8 different cytochromes via differentially element tagged antibodies and laser ablation ICP-MS, Analyst 138 (2013) 6309–6315.
[8] G.A. Qureshi, S.H. Parvez, Oxidative Stress and Neurodegenerative Disorders, Elsevier, Amsterdam, 2007 p719.
[9] O. Weinreb, S. Mandel, M.B.H. Youdim, T. Amit, Targeting dysregulation of brain iron homeostasis in Parkinson's disease by iron chelators, Free Radical Biology and Medicine 62 (2013) 52–64.
[10] Y.H. Hung, A.I. Bush, R.A. Cherny, Copper in the brain and Alzheimer's disease, Journal of Biological Inorganic Chemistry 15 (2010) 61–76.
[11] S. Sadiq, Z. Ghazala, A. Chowdhury, D. Busselberg, Metal toxicity at the synapse: presynaptic, postsynaptic, and long-term effects, Journal of Toxicology 2012 (2012) 132671.
[12] T. Narahashi, J.Y. Ma, O. Arakawa, E. Reuveny, M. Nakahiro, Gaba receptor-channel complex as a target site of mercury, mopper, zinc, and lanthanides, Cellular and Molecular Neurobiology 14 (1994) 599–621.
[13] J.A. Umbach, C.B. Gundersen, Mercuric ions are potent noncompetitive antagonists of human-brain kainate receptors expressed in xenopus oocytes, Molecular Pharmacology 36 (1989) 582–588.
[14] I.N. Sharonova, V.S. Vorobjev, H.L. Haas, High-affinity copper block of GABA (A) receptor-mediated currents in acutely isolated cerebellar Purkinje cells of the rat, European Journal of Neuroscience 10 (1998) 522–528.
[15] S. Majumdar, J.R. Peralta-Videa, H. Castillo-Michel, J. Hong, C.M. Rico, J.L. Gardea-Torresdey, Applications of synchrotron mu-XRF to study the distribution of biologically important elements in different environmental matrices: a review, Analytica Chimica Acta 755 (2012) 1–16.
[16] J. Vickerman, N. Winograd, Cluster TOF-SIMS imaging and the characterization of biological materials, in: C.M. Mahoney (Ed.), Cluster Secondary Ion Mass Spectrometry: Principles and Applications, J. Wiley, Hoboken, NJ, 2013, pp. 269–312.
[17] J.S. Becker, Inorganic Mass Spectrometry: Principles and Applications, John Wiley and Sons, Chichester, 2007.
[18] D.S. Gholap, A. Izmer, B. De Samber, J.T. van Elteren, V.S. Selih, R. Evens, K. De Schamphelaere, C. Janssen, L. Balcaen, I. Lindemann, L. Vincze, F. Vanhaecke,

Comparison of laser ablation-inductively coupled plasma-mass spectrometry and micro-X-ray fluorescence spectrometry for elemental imaging in Daphnia magna, Analytica Chimica Acta 664 (2010) 19–26.
[19] F. Blaske, O. Reifschneider, G. Gosheger, C.A. Wehe, M. Sperling, U. Karst, G. Hauschild, G. Höll, Elemental bioimaging of nanosilver-coated prostheses using X-ray fluorescence spectroscopy and laser ablation-inductively coupled plasma-mass spectrometry, Analytical Chemistry 86 (2014) 615–620.
[20] J.S. Becker, U. Breuer, H.F. Hsieh, T. Osterholt, U. Kumtabtim, B. Wu, A. Matusch, J. A. Caruso, Z.Y. Qin, Bioimaging of metals and biomolecules in mouse heart by laser ablation inductively coupled plasma mass spectrometry and secondary ion mass spectrometry, Analytical Chemistry 82 (2010) 9528–9533.
[21] I. Levèvre, K. Vogel-Mikus, L. Jeromel, P. Vavpetic, S. Planchon, I. Arcon, J.T. van Elteren, G. Lepoint, S. Gobert, J. Renaut, P. Pelicon, S. Lutts, Differential cadmium and zinc distribution in relation to their physiological impact in the leaves of the accumulating *Zygophyllum fabago* L, Plant Cell and Environment 37 (2014) 1299–1320.
[22] A. Matusch, C. Depboylu, C. Palm, B. Wu, G.U. Hoglinger, M.K.H. Schafer, J.S. Becker, Cerebral bioimaging of Cu, Fe, Zn, and Mn in the MPTP mouse model of Parkinson's disease using laser ablation inductively coupled plasma mass spectrometry (LA-ICP-MS), Journal of the American Society for Mass Spectrometry 21 (2010) 161–171.
[23] D.J. Hare, J.L. George, R. Grimm, S. Wilkins, P.A. Adlard, R.A. Cherny, A.I. Bush, D.I. Finkelstein, P. Doble, Three-dimensional elemental bio-imaging of Fe, Zn, Cu, Mn and P in a 6-hydroxydopamine lesioned mouse brain, Metallomics 2 (2010) 745–753.
[24] D.S. Urgast, O. Ou, M.J. Gordon, A. Raab, G.F. Nixon, I.S. Kwun, J.H. Beattie, J. Feldmann, Microanalytical isotope ratio measurements and elemental mapping using laser ablation ICP-MS for tissue thin sections: zinc tracer studies in rats, Analytical and Bioanalytical Chemistry 402 (2012) 287–297.
[25] N. Kamaly, J.A. Pugh, T.L. Kalber, J. Bunch, A.D. Miller, C.W. McLeod, J.D. Bell, Imaging of gadolinium spatial distribution in tumor tissue by laser ablation inductively coupled plasma mass spectrometry, Molecular Imaging and Biology 12 (2010) 361–366.
[26] B. Jackson, S. Harper, L. Smith, J. Flinn, Elemental mapping and quantitative analysis of Cu, Zn, and Fe in rat brain sections by laser ablation ICP-MS, Analytical and Bioanalytical Chemistry 384 (2006) 1618–2642.
[27] V. Trunova, A. Sidorina, V. Zvereva, B. Churin, Changes in the elemental content of rat heart as a result of the fixation in formalin analyzed by synchrotron radiation X-ray fluorescent analysis, Journal of Trace Elements in Medicine and Biology 27 (2013) 76–77.
[28] T. Moos, Simultaneous application of Timm's sulphide silver method and immunofluorescence histochemistry, Journal of Neuroscience Methods 48 (1993) 149–156.
[29] H. Boonstra, J.W. Oosterhuis, A.M. Oosterhuis, G.J. Fleuren, Cervical tissue shrinkage by formaldehyde fixation, paraffin wax embedding, section cutting and mounting, Virchows Archive a Pathological Anatomy and Histopathology 402 (1983) 195–201.
[30] D. Hare, C. Austin, P. Doble, Quantification strategies for elemental imaging of biological samples using laser ablation-inductively coupled plasma-mass spectrometry, Analyst 137 (2012) 1527–1537.
[31] D.J. Hare, J. Lear, D. Bishop, A. Beavis, P.A. Doble, Protocol for production of matrix-matched brain tissue standards for imaging by laser ablation-inductively coupled plasma-mass spectrometry, Analytical Methods-UK 5 (2013) 1915–1921.
[32] A. Matusch, L.S. Fenn, C. Depboylu, M. Klietz, S. Strohmer, J.A. McLean, J.S. Becker, Combined elemental and biomolecular mass spectrometry imaging for probing the inventory of tissue at a micrometer scale, Analytical Chemistry 84 (2012) 3170–3178.
[33] P. Cheajesadagul, W. Wananukul, A. Siripinyanond, J. Shiowatana, Metal doped keratin film standard for LA-ICP-MS determination of lead in hair samples, Journal of Analytical Atomic Spectrometry 26 (2011) 493–498.
[34] J.A.T. Pugh, A.G. Cox, C.W. McLeod, J. Bunch, B. Whitby, B. Gordon, T. Kalber, E. White, A novel calibration strategy for analysis and imaging of biological thin sections by laser ablation inductively coupled plasma mass spectrometry, Journal of Analytical Atomic Spectrometry 26 (2011) 1667–1673.
[35] M. Debeljak, J.T. van Elteren, K. Vogel-Mikus, Development of a 2D laser ablation inductively coupled plasma mass spectrometry mapping procedure for mercury in maize (*Zea mays* L.) root cross-sections, Analytica Chimica Acta 787 (2013) 155–162.
[36] H. Sela, Z. Karpas, H. Cohen, Y. Zakon, Y. Zeiri, Preparation of stable standards of biological tissues for laser ablation analysis, International Journal of Mass Spectrometry 307 (2011) 142–148.
[37] D.J. Hare, J.K. Lee, A.D. Beavis, A. van Gramberg, J. George, P.A. Adlard, D.I. Finkelstein, P.A. Doble, Three-Dimensional atlas of iron, copper, and zinc in the mouse cerebrum and brainstem, Analytical Chemistry 84 (2012) 3990–3997.
[38] D. Hare, B. Reedy, R. Grimm, S. Wilkins, I. Volitakis, J.L. George, R.A. Cherny, A.I. Bush, D.I. Finkelstein, P. Doble, Quantitative elemental bio-imaging of Mn, Fe, Cu and Zn in 6-hydroxydopamine induced Parkinsonism mouse models, Metallomics 1 (2009) 53–58.
[39] J. Koelmel, T. Leland, H. Wang, D. Amarasiriwardena, B. Xing, Investigation of gold nanoparticles uptake and their tissue level distribution in rice plants by laser ablation-inductively coupled-mass spectrometry, Environmental Pollution 174 (2013) 222–228.
[40] C. Austin, T.M. Smith, A. Bradman, K. Hinde, R. Joannes-Boyau, D. Bishop, D.J. Hare, P. Doble, B. Eskenazi, M. Arora, Barium distributions in teeth reveal early-life dietary transitions in primates, Nature 498 (2013) 216–220.
[41] D.A. Frick, D. Gunther, Fundamental studies on the ablation behaviour of carbon in LA-ICP-MS with respect to the suitability as internal standard, Journal of Analytical Atomic Spectrometry 27 (2012) 1294–1303.
[42] J.S. Becker, A. Matusch, C. Palm, D. Salber, K.A. Morton, S. Becker, Bioimaging of metals in brain tissue by laser ablation inductively coupled plasma mass spectrometry (LA-ICP-MS) and metallomics, Metallomics 2 (2010) 104–111.
[43] D. Pozebon, V.L. Dressler, M.F. Mesko, A. Matusch, J.S. Becker, Bioimaging of metals in thin mouse brain section by laser ablation inductively coupled plasma mass spectrometry: novel online quantification strategy using aqueous standards, Journal of Analytical Atomic Spectrometry 25 (2010) 1739–1744.
[44] C. Austin, D. Hare, T. Rawling, A.M. McDonagh, P. Doble, Quantification method for elemental bio-imaging by LA-ICP-MS using metal spiked PMMA films, Journal of Analytical Atomic Spectrometry 25 (2010) 722–725.
[45] I. Konz, B. Fernandez, M.L. Fernandez, R. Pereiro, H. Gonzalez, L. Alvarez, M. Coca-Prados, A. Sanz-Medel, Gold internal standard correction for elemental imaging of soft tissue sections by LA-ICP-MS: element distribution in eye microstructures, Analytical and Bioanalytical Chemistry 405 (2013) 3091–3096.
[46] R.W. Hutchinson, A.G. Cox, C.W. McLeod, P.S. Marshall, A. Harper, E.L. Dawson, D.R. Howlett, Imaging and spatial distribution of beta-amyloid peptide and metal ions in Alzheimer's plaques by laser ablation-inductively coupled plasma-mass spectrometry, Analytical Biochemistry 346 (2005) 225–233.
[47] T. Osterholt, D. Salber, A. Matusch, J.S. Becker, C. Palm, IMAGENA: image generation and analysis – an interactive software tool handling LA-ICP-MS data, International Journal of Mass Spectrometry 307 (2011) 232–239.
[48] B.P. Jackson, D. Bugge, J.F. Ranville, C.Y. Chen, Bioavailability, toxicity, and bioaccumulation of quantum dot nanoparticles to the amphipod leptocheirus plumulosus, Environmental Science and Technology 46 (2012) 5550–5556.
[49] H.A. Wang, D. Grolimund, C. Giesen, C.N. Borca, J.R. Shaw-Stewart, B. Bodenmiller, D. Gunther, Fast chemical imaging at high spatial resolution by laser ablation inductively coupled plasma mass spectrometry, Analytical Chemistry 85 (2013) 10107–10116.
[50] D. Fliegel, C. Frei, G. Fontaine, Z.C. Hu, S. Gao, D. Gunther, Sensitivity improvement in laser ablation inductively coupled plasma mass spectrometry achieved using a methane/argon and methanol/water/argon mixed gas plasma, Analyst 136 (2011) 4925–4934.
[51] I.L. Turner, Inductively coupled plasma spectroscopy, USA (1993).
[52] J. Lear, D.J. Hare, F. Fryer, P.A. Adlard, D.I. Finkelstein, P.A. Doble, High-resolution elemental bioimaging of Ca, Mn, Fe, Co, Cu, and Zn employing LA-ICP-MS and hydrogen reaction gas, Analytical Chemistry 84 (2012) 6707–6714.
[53] M.A. da Silva, M.A. Arruda, Laser ablation (imaging) for mapping and determining Se and S in sunflower leaves, Metallomics 5 (2013) 62–67.
[54] C. Giesen, H.A. Wang, D. Schapiro, N. Zivanovic, A. Jacobs, B. Hattendorf, P.J. Schuffler, D. Grolimund, J.M. Buhmann, S. Brandt, Z. Varga, P.J. Wild, D. Gunther, B. Bodenmiller, Highly multiplexed imaging of tumor tissues with subcellular resolution by mass cytometry, Nature Methods 11 (2014) 417–422.
[55] M. Zoriy, A. Matusch, T. Spruss, J.S. Becker, Laser ablation inductively coupled plasma mass spectrometry for imaging of copper, zinc, and platinum in thin sections of a kidney from a mouse treated with cis-platin, International Journal of Mass Spectrometry 260 (2007) 102–106.
[56] T.H. Wang, C.H. Jian, Y.K. Hsieh, F.N. Wang, C.F. Wang, Spatial distributions of inorganic elements in honeybees (*Apis mellifera* L.) and possible relationships to dietary habits and surrounding environmental pollutants, Journal of Agricultural and Food Chemistry 61 (2013) 5009–5015.
[57] P. Nemes, A.A. Barton, Y. Li, A. Vertes, Ambient molecular imaging and depth profiling of live tissue by infrared laser ablation electrospray ionization mass spectrometry, Analytical Chemistry 80 (2008) 4575–4582.
[58] E. Moreno-Gordaliza, C. Giesen, A. Lazaro, D. Esteban-Fernandez, B. Humanes, B. Canas, U. Panne, A. Tejedor, N. Jakubowski, M.M. Gomez-Gomez, Elemental bioimaging in kidney by LA-ICP-MS as a tool to study nephrotoxicity and renal protective strategies in cisplatin therapies, Analytical Chemistry 83 (2011) 7933–7940.
[59] I. Horn, D. Gunther, The influence of ablation carrier gasses Ar, He and Ne on the particle size distribution and transport efficiencies of laser ablation-induced aerosols: implications for LA-ICP-MS, Applied Surface Science 207 (2003) 144–157.
[60] J. Koch, M. Walle, S. Schlamp, T. Rosgen, D. Gunther, Expansion phenomena of aerosols generated by laser ablation under helium and argon atmosphere, Spectrochimica Acta B 63 (2008) 37–41.
[61] I. Konz, B. Fernández, M.L. Fernandez, R. Pereiro, A. Sanz-Medel, Design and evaluation of a new Peltier-cooled laser ablation cell with on-sample temperature control, Analytica Chimica Acta 809 (2014) 88–96.
[62] I. Konz, B. Fernandez, M.L. Fernandez, R. Pereiro, H. González-Iglesias, M. Coca-Prados, A. Sanz-Medel, Quantitative bioimaging of trace elements in the human lens by LA-ICP-MS, Analytical and Bioanalytical Chemistry 406 (2014) 2343–2348.
[63] B. Wu, J.S. Becker, Bioimaging of metals in rat brain hippocampus by laser microdissection inductively coupled plasma mass spectrometry (LMD-ICP-MS) using high-efficiency laser ablation chambers, International Journal of Mass Spectrometry 323 (2012) 34–40.
[64] E. White, A. Bienemann, J. Pugh, E. Castrique, M. Wyatt, H. Taylor, A. Cox, C. Mcleod, S. Gill, An evaluation of the safety and feasibility of convection-enhanced delivery of carboplatin into the white matter as a potential treatment for high-grade glioma, Journal of Neuro-Oncology 108 (2012) 77–88.

[65] J.A.T. Pugh, A.G. Cox, C.W. McLeod, J. Bunch, M.J. Writer, S.L. Hart, A. Bienemann, E. White, J. Bell, Elemental imaging of MRI contrast agents: benchmarking of LA-ICP-MS to MRI, Analytical and Bioanalytical Chemistry 403 (2012) 1641–1649.
[66] G.D. Kenny, A.S. Bienemann, A.D. Tagalakis, J.A. Pugh, K. Welser, F. Campbell, A.B. Tabor, H.C. Hailes, S.S. Gill, M.F. Lythgoe, C.W. McLeod, E.A. White, S.L. Hart, Multifunctional receptor-targeted nanocomplexes for the delivery of therapeutic nucleic acids to the Brain, Biomaterials 34 (2013) 9190–9200.
[67] J.S. Becker, J. Dobrowolska, M. Zoriy, A. Matusch, Imaging of uranium on rat brain sections using LA-ICP-MS: a new tool for the study of critical substructures affined to heavy metals in tissues, Rapid Communications in Mass Spectrometry 22 (2008) 2768–2772.
[68] J.S. Becker, A. Matusch, J.S. Becker, B. Wu, C. Palm, A.J. Becker, D. Salber, Mass spectrometric imaging (MSI) of metals using advanced BrainMet techniques for biomedical research, International Journal of Mass Spectrometry 307 (2011) 3–15.
[69] J.S. Becker, M. Zoriy, B. Wu, A. Matusch, B.J. Su, Imaging of essential and toxic elements in biological tissues by LA-ICP-MS, Journal of Analytical Atomic Spectrometry 23 (2008) 1275–1280.
[70] A. Matusch, S. Becker, Bio-imaging of metals in a mouse model of Alzheimer's disease by laser ablation inductively coupled plasma mass spectrometry, Biomedical Spectroscopy and Imaging 1 (2012) 57–65.
[71] A. Sussulini, A. Matusch, M. Klietz, A. Bauer, C. Depboylu, J.S. Becker, Quantitative imaging of Cu, Fe, Mn and Zn in the L-DOPA-treated unilateral 6-hydroxydopamine Parkinson's disease mouse model by LA-ICP-MS, Biomedical Spectroscopy and Imaging 1 (2012) 125–136.
[72] L.M. Wang, J.S. Becker, Q. Wu, M.F. Oliveira, F.A. Bozza, A.L. Schwager, J.M. Hoffman, K.A. Morton, Bioimaging of copper alterations in the aging mouse brain by autoradiography, laser ablation inductively coupled plasma mass spectrometry and immunohistochemistry, Metallomics 2 (2010) 348–353.
[73] M. Zoriy, M. Dehnhardt, A. Matusch, J.S. Becker, Comparative imaging of P, S, Fe, Cu Zn and C in thin sections of rat brain tumor as well as control tissues by laser ablation inductively coupled plasma mass spectrometry, Spectrochimica Acta B 63 (2008) 375–382.
[74] G. Paxinos, K.B.J. Franklin, The Mouse Brain in Stereotaxic Coordinates, Academic Press, San Diego, 2001.
[75] J.S. Becker, U. Kumtabtim, B. Wu, P. Steinacker, M. Otto, A. Matusch, Mass spectrometry imaging (MSI) of metals in mouse spinal cord by laser ablation ICP-MS, Metallomics 4 (2012) 284–288.
[76] O. Reifschneider, C.A. Wehe, K. Diebold, C. Becker, M. Sperling, U. Karst, Elemental bioimaging of haematoxylin and eosin-stained tissues by laser ablation ICP-MS, Journal of Analytical Atomic Spectrometry 28 (2013) 989–993.
[77] J. Seuma, J. Bunch, A. Cox, C. McLeod, J. Bell, C. Murray, Combination of immunohistochemistry and laser ablation ICP mass spectrometry for imaging of cancer biomarkers, Proteomics 8 (2008) 3775–3784.
[78] D. Hare, F. Burger, C. Austin, F. Fryer, R. Grimm, B. Reedy, R.A. Scolyer, J.F. Thompson, P. Doble, Elemental bio-imaging of melanoma in lymph node biopsies, Analyst 134 (2009) 450–453.
[79] A. Matusch, A. Bauer, J.S. Becker, Element imaging in formalin fixed slices of human mesencephalon, International Journal of Mass Spectrometry 307 (2011) 240–244.
[80] J.S. Becker, M. Zoriy, C. Pickhardt, N. Palomero-Gallagher, K. Zilles, Imaging of copper, zinc, and other elements in thin section of human brain samples (Hippocampus) by laser ablation inductively coupled plasma mass spectrometry, Analytical Chemistry 77 (2005) 3208–3216.
[81] J. Dobrowolska, M. Dehnhardt, A. Matusch, M. Zoriy, P. Koscielniak, K. Zilles, J. S. Becker, Quantitative imaging of zinc, copper and lead in three distinct regions of the human brain by laser ablation inductively coupled plasma mass spectrometry, Talanta 74 (2008) 717–723.
[82] J.S. Becker, R.C. Dietrich, A. Matusch, D. Pozebon, V.L. Dressier, Quantitative images of metals in plant tissues measured by laser ablation inductively coupled plasma mass spectrometry, Spectrochimica Acta B 63 (2008) 1248–1252.
[83] B. Wu, Y.X. Chen, J.S. Becker, Study of essential element accumulation in the leaves of a Cu-tolerant plant *Elsholtzia splendens* after Cu treatment by imaging laser ablation inductively coupled plasma mass spectrometry (LA-ICP-MS), Analytica Chimica Acta 633 (2009) 165–172.
[84] Y. Zhu, A. Hioki, A. Itoh, T. Umemura, H. Haraguchi, K. Chiba, Relative enrichment of Mo in the radicle of peanut seed (*Arachis hypogaea*), observed by multi-elemental imagining with LA-ICP-MS, Analytical Sciences 28 (2012) 1121–1124.
[85] B. Wu, F. Andersch, W. Weschke, H. Weber, J.S. Becker, Diverse accumulation and distribution of nutrient elements in developing wheat grain studied by laser ablation inductively coupled plasma mass spectrometry imaging, Metallomics 5 (2013) 1276–1284.
[86] H. Bortels, Molybdän als katalysator bei der biologischen stickstoffbindung, Archiv für Mikrobiologie 1 (1930) 333–342.
[87] S.P. Singh, K. Vogel-Mikus, I. Arcon, P. Vavpetic, L. Jeromel, P. Pelicon, J. Kumar, R. Tuli, Pattern of iron distribution in maternal and filial tissues in wheat grains with contrasting levels of iron, Journal of Experimental Botany 64 (2013) 3249–3260.
[88] J.S. Becker, A. Matusch, C. Depboylu, J. Dobrowolska, M. Zoriy, Quantitative imaging of selenium, copper, and zinc in thin sections of biological tissues (Slugs–Genus arion) measured by laser ablation inductively coupled of plasma mass spectrometry, Analytical Chemistry 79 (2007) 6074–6080.
[89] M.R. Florez, M. Aramendia, M. Resano, A.C. Lapena, L. Balcaen, F. Vanhaecke, Isotope ratio mapping by means of laser ablation-single collector-ICP-mass spectrometry: Zn tracer studies in thin sections of Daphnia magna, Journal of Analytical Atomic Spectrometry 28 (2013) 1005–1015.
[90] M.M. Pornwilard, R. Weiskirchen, N. Gassler, A.K. Bosserhoff, J.S. Becker, Novel bioimaging techniques of metals by laser ablation inductively coupled plasma mass spectrometry for diagnosis of fibrotic and cirrhotic liver disorders, PLoS One 8 (2013).
[91] C. Austin, D. Hare, A.L. Rozelle, W.H. Robinson, R. Grimm, P. Doble, Elemental bio-imaging of calcium phosphate crystal deposits in knee samples from arthritic patients, Metallomics 1 (2009) 142–147.
[92] M. Siebold, P. Leidich, M. Bertini, G. Deflorio, J. Feldmann, E.M. Krupp, E. Halmschlager, S. Woodward, Application of elemental bioimaging using laser ablation ICP-MS in forest pathology: distribution of elements in the bark of *Picea sitchensis* following wounding, Analytical and Bioanalytical Chemistry 402 (2012) 3323–3331.
[93] B.D. Corbin, E.H. Seeley, A. Raab, J. Feldmann, M.R. Miller, V.J. Torres, K.L. Anderson, B.M. Dattilo, P.M. Dunman, R. Gerads, R.M. Caprioli, W. Nacken, W.J. Chazin, E.P. Skaar, Metal chelation and inhibition of bacterial growth in tissue abscesses, Science 319 (2008) 962–965.
[94] A.B. Moradi, S. Swoboda, B. Robinson, T. Prohaska, A. Kaestner, S.E. Oswald, W. W. Wenzel, R. Schulin, Mapping of nickel in root cross-sections of the hyperaccumulator plant *Berkheya coddii* using laser ablation ICP-MS, Environmental and Experimental Botany 69 (2010) 24–31.
[95] J. Koelmel, D. Amarasiriwardena, Imaging of metal bioaccumulation in hay-scented fern (*Dennstaedtia punctilobula*) rhizomes growing on contaminated soils by laser ablation ICP-MS, Environmental Pollution 168 (2012) 62–70.
[96] R. Han, M. Quinet, E. Andre, J.T. van Elteren, F. Destrebecq, K. Vogel-Mikus, G. Cui, M. Debeljak, I. Lefevre, S. Lutts, Accumulation and distribution of Zn in the shoots and reproductive structures of the halophyte plant species *Kosteletzkya virginica* as a function of salinity, Planta 238 (2013) 441–457.
[97] H.X. Yang, L.H. Zhao, J.X. Gao, W. Liu, B. Li, Bioimaging and distribution of Cd, P, S, K, Ca, Cu and Zn elements in Indian mustard stem, Chinese Journal of Analytical Chemistry 42 (2014) 355–359.
[98] O. Reifschneider, C.A. Wehe, I. Raj, J. Ehmcke, G. Ciarimboli, M. Sperling, U. Karst, Quantitative bioimaging of platinum in polymer embedded mouse organs using laser ablation ICP-MS, Metallomics 5 (2013) 1440–1447.
[99] C. Herdering, C.A. Wehe, O. Reifschneider, I. Raj, G. Ciarimboli, K. Diebold, C. Becker, M. Sperling, U. Karst, Laser ablation based bioimaging with simulaneous elemental and molecular spectrometry: towards spatially resolved speciation analysis, Rapid Communications in Mass Spectrometry 27 (2013) 2588–2594.
[100] Y.K. Hsieh, P.S. Jiang, B.S. Yang, T.Y. Sun, H.H. Peng, C.F. Wang, Using laser ablation/inductively coupled plasma mass spectrometry to bioimage multiple elements in mouse tumors after hyperthermia, Analytical and Bioanalytical Chemistry 401 (2011) 909–915.
[101] T. Wang, H. Hsieh, Y. Hsieh, C. Chiang, Y. Sun, C. Wang, The in vivo biodistribution and fate of CdSe quantum dots in the murine model: a laser ablation inductively coupled plasma mass spectrometry study, Analytical and Bioanalytical Chemistry 404 (2012) 3025–3036.
[102] D. Drescher, C. Giesen, H. Traub, U. Panne, J. Kneipp, N. Jakubowski, Quantitative imaging of gold and silver nanoparticles in single eukaryotic cells by laser ablation ICP-MS, Analytical Chemistry 84 (2012) 9684–9688.
[103] A. Izmer, D. Gholap, K. De Houwer, F. Cuyckens, F. Vanhaecke, A pilot study on the use of laser ablation-ICP-mass spectrometry for assessing/mapping the distribution of a drug and its metabolites across the body compartments of rats, Journal of Analytical Atomic Spectrometry 27 (2012) 413–418.
[104] D.S. Urgast, D.G. Ellingsen, B. Berlinger, E. Eilertsen, G. Friisk, V. Skaug, Y. Thomassen, J.H. Beattie, I.S. Kwun, J. Feldmann, Multi-elemental bio-imaging of rat tissue from a study investigating the bioavailability of bismuth from shotgun pellets, Analytical and Bioanalytical Chemistry 404 (2012) 89–99.
[105] D. Hare, S. Tolmachev, A. James, D. Bishop, C. Austin, F. Fryer, P. Doble, Elemental bio-imaging of thorium, uranium, and plutonium in tissues from occupationally exposed former nuclear workers, Analytical Chemistry 82 (2010) 3176–3182.
[106] M.C. Santos, M. Wagner, B. Wu, J. Scheider, J. Oehlmann, S. Cadore, J.S. Becker, Biomonitoring of metal contamination in a marine prosobranch snail (Nassarius reticulatus) by imaging laser ablation inductively coupled plasma mass spectrometry (LA-ICP-MS), Talanta 80 (2009) 428–433.
[107] C. Giesen, T. Mairinger, L. Khoury, L. Waentig, N. Jakubowski, U. Panne, Multiplexed immunohistochemical detection of tumor markers in breast cancer tissue using laser ablation inductively coupled plasma mass spectrometry, Analytical Chemistry 83 (2011) 8177–8183.
[108] C. Giesen, L. Waentig, T. Mairinger, D. Drescher, J. Kneipp, P.H. Roos, U. Panne, N. Jakubowski, Iodine as an elemental marker for imaging of single cells and tissue sections by laser ablation inductively coupled plasma mass spectrometry, Journal of Analytical Atomic Spectrometry 26 (2011) 2160–2165.
[109] A. Sussulini, E. Wiener, T. Marnitz, B. Wu, B. Muller, B. Hamm, J.S. Becker, Quantitative imaging of the tissue contrast agent [Gd(DTPA)](2−) in articular cartilage by laser ablation inductively coupled plasma mass spectrometry, Contrast Media & Molecular Imaging 8 (2013) 204–209.
[110] D. Hare, C. Austin, P. Doble, M. Arora, Elemental bio-imaging of trace elements in teeth using laser ablation-inductively coupled plasma-mass spectrometry, Journal of Dentistry 39 (2011) 397–403.
[111] A.E. Dolphin, A.H. Goodman, D.D. Amarasiriwardena, Variation in elemental intensities among teeth and between pre- and postnatal regions of enamel, American Journal of Physical Anthropology 128 (2005) 878–888.

[112] J. Santner, H. Zhang, D. Leitner, A. Schnepf, T. Prohaska, M. Puschenreiter, W. W. Wenzel, High-resolution chemical imaging of labile phosphorus in the rhizosphere of *Brassica napus* L. cultivars, Environmental and Experimental Botany 77 (2012) 219–226.
[113] B.D. Barst, A.K. Gevertz, M.M. Chumchal, J.D. Smith, T.R. Rainwater, P.E. Drevnick, K.E. Hudelson, A. Hart, G.F. Verbeck, A.P. Roberts, Laser ablation ICP-MS co-localization of mercury and immune response in fish, Environmental Science and Technology 45 (2011) 8982–8988.
[114] M. Arora, D. Hare, C. Austin, D.R. Smith, P. Doble, Spatial distribution of manganese in enamel and coronal dentine of human primary teeth, Science of the Total Environment 409 (2011) 1315–1319.
[115] S.C. Veasey, J. Lear, Y. Zhu, J.B. Grinspan, D.J. Hare, S.H. Wang, D. Bunch, P.A. Doble, S.R. Robinson, Long-term intermittent hypoxia elevates cobalt levels in the brain and injures white matter in adult mice, Sleep 36 (2013) 1471–1481.
[116] S. Grosse Brinkhaus, J. Bornhorst, S. Chakraborty, C.A. Wehe, R. Niehaus, O. Reifschneider, M. Aschner, U. Karst, Elemental bioimaging of manganese uptake in *C. elegans*, Metallomics 6 (2014) 617–621.
[117] M. Galiova, J. Kaiser, K. Novotny, M. Hartl, R. Kizek, P. Babula, Utilization of laser-assisted analytical methods for monitoring of lead and nutrition elements distribution in fresh and dried *Capsicum annuum* L. leaves, Microscopy Research and Technique 74 (2011) 845–852.
[118] J.S. Becker, M. Zoriy, M. Dehnhardt, C. Pickhardt, K. Zilles, Copper, zinc, phosphorus and sulfur distribution in thin section of rat brain tissues measured by laser ablation inductively coupled plasma mass spectrometry: possibility for small-size tumor analysis, Journal of Analytical Atomic Spectrometry 20 (2005) 912–917.
[119] M.V. Zoriy, M. Dehnhardt, G. Reifenberger, K. Zilles, J.S. Becker, Imaging of Cu, Zn, Pb and U in human brain tumor resections by laser ablation inductively coupled plasma mass spectrometry, International Journal of Mass Spectrometry 257 (2006) 27–33.
[120] M.V. Zoriy, J.S. Becker, Imaging of elements in thin cross sections of human brain samples by LA-ICP-MS: a study on reproducibility, International Journal of Mass Spectrometry 264 (2007) 175–180.
[121] J.S. Becker, M. Zoriy, J.S. Becker, J. Dobrowolska, A. Matusch, Imaging mass spectrometry by laser ablation inductively coupled plasma mass spectrometry in biological tissues and proteomics, Journal of Analtical Atomic Spectrometry 22 (2007) 736–744.
[122] B. Wu, M. Zoriy, Y.X. Chen, J.S. Becker, Imaging of nutrient elements in the leaves of *Elsholtzia splendens* by laser ablation inductively coupled plasma mass spectrometry (LA-ICP-MS), Talanta 78 (2009) 132–137.
[123] J.S. Becker, M. Zoriy, A. Matusch, B. Wu, D. Salber, C. Palm, J.S. Becker, Bioimaging of metals by laser ablation inductively coupled plasma mass spectrometry (LA-ICP-MS), Mass Spectrometry Reviews 29 (2010) 156–175.
[124] J.S. Becker, D. Salber, New mass spectrometric tools in brain research, TrAC Trends in Analytical Chemistry 29 (2010) 966–979.
[125] A.M. Oros-Peusquens, A. Matusch, J.S. Becker, N.J. Shah, Automatic segmentation of tissue sections using the multielement information provided by LA-ICP-MS imaging and k-means cluster analysis, International Journal of Mass Spectrometry 307 (2011) 245–252.
[126] M.M. Pornwilard, U. Merle, R. Weiskirchen, J.S. Becker, Bioimaging of copper deposition in Wilson's disease mouse liver by laser ablation inductively coupled plasma mass spectrometry imaging (LA-ICP-MSI), International Journal of Mass Spectrometry 354-355 (2013) 281–287.
[127] B. Wu, S. Niehren, J.S. Becker, Mass spectrometric imaging of elements in biological tissues by new BrainMet technique-laser microdissection inductively coupled plasma mass spectrometry (LMD-ICP-MS), Journal of Analytical Atomic Spectrometry 26 (2011) 1653–1659.